nature communications

Article

https://doi.org/10.1038/s41467-024-52914-1

Non-averaged single-molecule tertiary structures reveal RNA self-folding through individual-particle cryo-electron tomography

Received: 22 December 2023

Accepted: 23 September 2024

Published online: 21 October 2024

Check for updates

Jianfang Liu[1], Ewan K. S. McRae[2,3], Meng Zhang[1,4], Cody Geary[2,5], Ebbe Sloth Andersen[2] ✉ & Gang Ren[1] ✉

Large-scale and continuous conformational changes in the RNA self-folding process present significant challenges for structural studies, often requiring trade-offs between resolution and observational scope. Here, we utilize individual-particle cryo-electron tomography (IPET) to examine the post-transcriptional self-folding process of designed RNA origami 6-helix bundle with a clasp helix (6HBC). By avoiding selection, classification, averaging, or chemical fixation and optimizing cryo-ET data acquisition parameters, we reconstruct 120 three-dimensional (3D) density maps from 120 individual particles at an electron dose of no more than 168 $e^{-}Å^{-2}$, achieving averaged resolutions ranging from 23 to 35 Å, as estimated by Fourier shell correlation (FSC) at 0.5. Each map allows us to identify distinct RNA helices and determine a unique tertiary structure. Statistical analysis of these 120 structures confirms two reported conformations and reveals a range of kinetically trapped, intermediate, and highly compacted states, demonstrating a maturation folding landscape likely driven by helix-helix compaction interactions.

The ancient Greek philosopher Heraclitus famously stated, "No man ever steps in the same river twice, for it's not the same river and he's not the same man." Similarly, during the post-transcriptional self-folding process of RNA in an aqueous environment at physiological temperature, RNA molecules exhibit kinetic and thermodynamic behaviors, undergoing continuous conformational changes with multidimensional flexibilities. In this dynamic context, each RNA molecule never assumes exactly the same structure twice, either over time or compared to other molecules at any given moment. Under these circumstances, an ideal approach to investigate molecular structures during the folding process would involve flash-freezing their structures at a single point in time and then imaging them one by one to determine the structure of each individual molecule without selection, classification, or averaging among different molecules.

Cryogenic electron microscopy (cryo-EM) offers the unique capability to image the projection of a single macromolecule embedded in vitrified ice from a single-tilt view, while cryogenic electron tomography (cryo-ET) provides a 3D structure by viewing a targeted single molecule from a series of tilt angles. However, the super low signal from a single molecule often poses challenges for 3D reconstruction. In such a situation, a common strategy is to select a homogeneous population (usually ~10–20% of the data) from a vast pool of heterogeneous molecules and average them into a single, static 3D structure. This averaging process has successfully achieved near-atomic

[1]The Molecular Foundry, Lawrence Berkeley National Laboratory, Berkeley, CA 94720, USA. [2]Interdisciplinary Nanoscience Center (iNANO), Aarhus University, DK-8000 Aarhus, Denmark. [3]Center for RNA Therapeutics, Houston Methodist Research Institute, Houston, TX 77030, USA. [4]California Institute for Quantitative Biosciences, University of California, Berkeley, CA 94720, USA. [5]Center for Molecular Biology of Heidelberg University (ZMBH), Heidelberg University, 69120 Heidelberg, Germany. ✉e-mail: esa@inano.au.dk; gren@lbl.gov

resolution structures of numerous protein molecules and complexes[1–3], including the ribosome in bacterial cell[4], through data analysis techniques like cryo-EM single-particle averaging (SPA) analysis[5] and cryo-ET subtomogram averaging[4]. However, the averaged structures often exhibit an anisotropic distribution of resolution[6] and may lose flexible domains[7]. For the molecules in relatively higher energy state, with lower homogeneity, significant flexibility, and continuous conformational changes[8–10]—such as DNA/RNA strings, nucleosome fibers[11], antibody flexibilities, lipoprotein structural varieties, and intrinsically disordered proteins (IDPs)[12]— the averaging methods often fail or are overlooked in structural determination. Achieving even a low-resolution structure through averaging remains challenging for these cases.

Determining the 3D structure of a single-molecule particle without averaging remains challenging[13] due to its small physical size, low signal-to-noise ratio (SNR), and the need to limit the electron dose to prevent radiation damage[14]. Consequently, cryo-ET is typically employed to study the non-averaged structure of large biological objects, such as bacteria[15] and cell sections[16], at low resolution. Theoretical predictions suggest that the resolution limit for a non-averaged single-molecule structure is ~15–20 Å[17,18].

To advance the cryo-ET technique for studying macromolecular structures without averaging, we have developed the individual-particle electron tomography (IPET) method[19], which benefits from focused electron tomography reconstruction (FETR) algorithms. This approach, combined with the development of a missing-wedge correction method[20] and the optimization of experimental and image processing protocols[21,22], has enabled us to characterize the structural varieties of several flexible molecules at low resolution, including lipoproteins[23,24] and DNA/RNA origami nanostructures[25,26].

To enhance the resolution of IPET, we meticulously refined the experimental conditions, including optimized electron dose, image tilting steps, sample preparation protocols, and image processing details. These enhancements were aimed to accurately capture the tertiary structures of an individual RNA origami particle. Unlike DNA origami nanostructure[27], which folds through heat annealing to reach a thermodynamic equilibrium, RNA origami was engineered as a single-stranded architecture[28]. This design facilitates isothermal folding during transcription by RNA polymerase[29], followed by a non-equilibrium self-folding process after synthesis (Fig. 1a)[30], often resulting in structures that significantly diverge from the global minimum free-energy state[31].

Given the complexities of RNA folding paths, including the influential role of noncanonical base-pair interactions and folding chaperones[32], studying endogenous RNAs presents considerable challenges. To navigate these complexities, we utilize rationally designed RNA nanostructures, i.e., cotranscriptional folding RNA origami (six-helix bundle with a clasp helix, 6HBC)[29]. These systems offer simplified post-synthesis frameworks that incorporate non-equilibrium elements, such as folding traps and maturation processes[28,33]. This approach allows us to effectively study the dynamic folding landscapes of RNA, shedding light on both the predictable and unpredictable aspects of RNA structure formation.

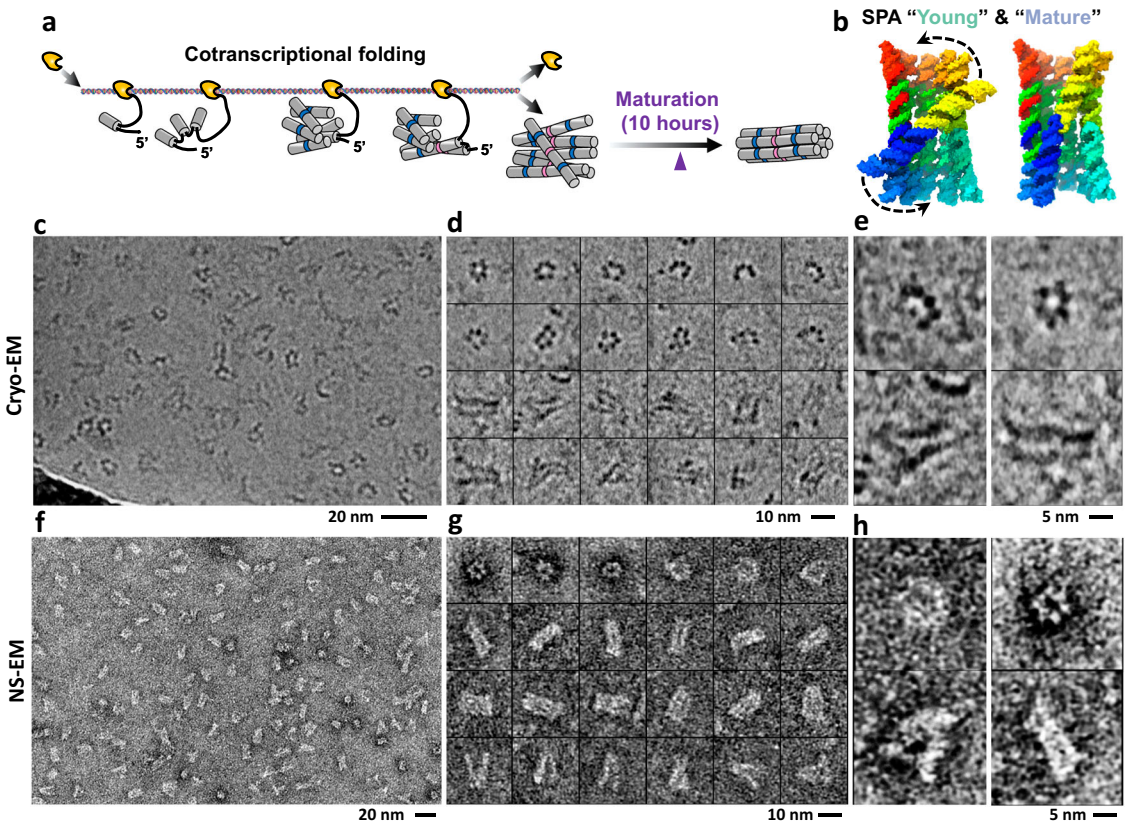

Fig. 1 | RNA origami folding process and EM images. a A schematic illustrating the transcriptional folding and maturation processes of an RNA origami 6-helix bundle with clasp (6HBC). Cryo-ET grids were prepared six hours after transcription, as indicated by the purple triangle. **b** Two subnanometer-resolution structures of 6HBC, "young" (7PTK) and "mature" (7PTL), determined by the cryo-EM single-particle averaging (SPA) analysis method[33]. The structures are colored from 5′ (blue) to 3′ (red), with arrows indicating the proposed self-folding maturation mechanism. **c** A survey cryo-EM image of the RNA 6HBC sample. **d** Twenty-four representative particles. **e** Zoomed-in images of four representative particles, including two top views showing helical bundles in open and closed conformations, and two side views showing the conformations in open and closed stages. **f** A survey NS-EM image of the same sample. **g** Twenty-four representative particles. **h** Zoomed-in images of four representative particles showing the open and closed conformations from two perpendicular views.

https://doi.org/10.1038/s41467-024-52914-1

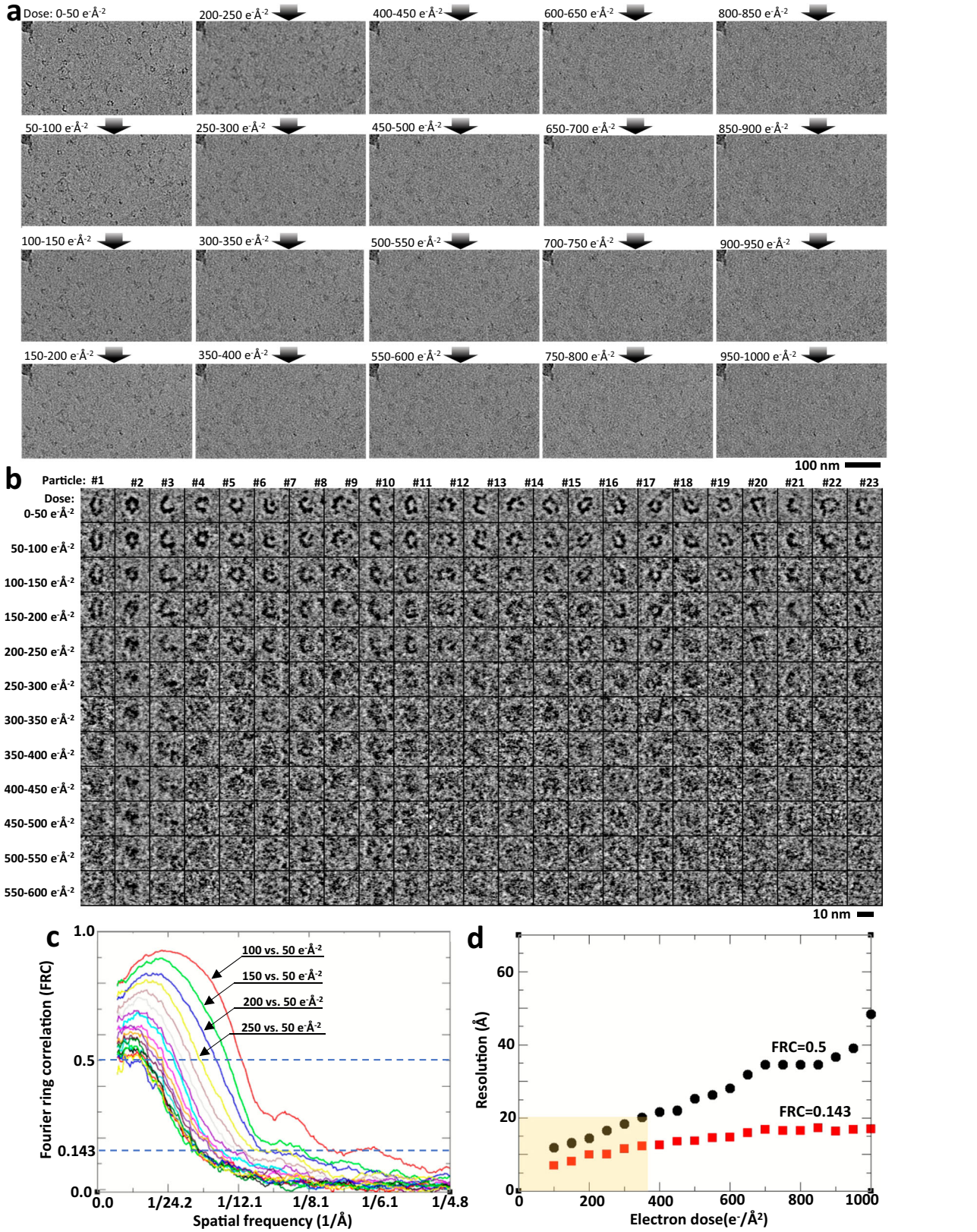

Fig. 2 | The effect of electron dose on cryo-EM images of 6HBC RNA particles. a A sample area was sequentially imaged with a dose of 50 $e^{-}Å^{-2}$ for 20 iterations. The images correspond to radiation damage with an accumulated dose of 50, 100, 150, and up to 1000 $e^{-}Å^{-2}$, respectively. **b** Zoomed-in images of 23 representative areas containing particles. **c** Fourier ring correlation (FRC) curves showing the effects of radiation damage, with each curve calculated by comparing the first image (50 $e^{-}Å^{-2}$) against the subsequent images. **d** A plot of FRC frequencies at FRC = 0.5 and 0.143, respectively, against their corresponding radiation doses.

https://doi.org/10.1038/s41467-024-52914-1

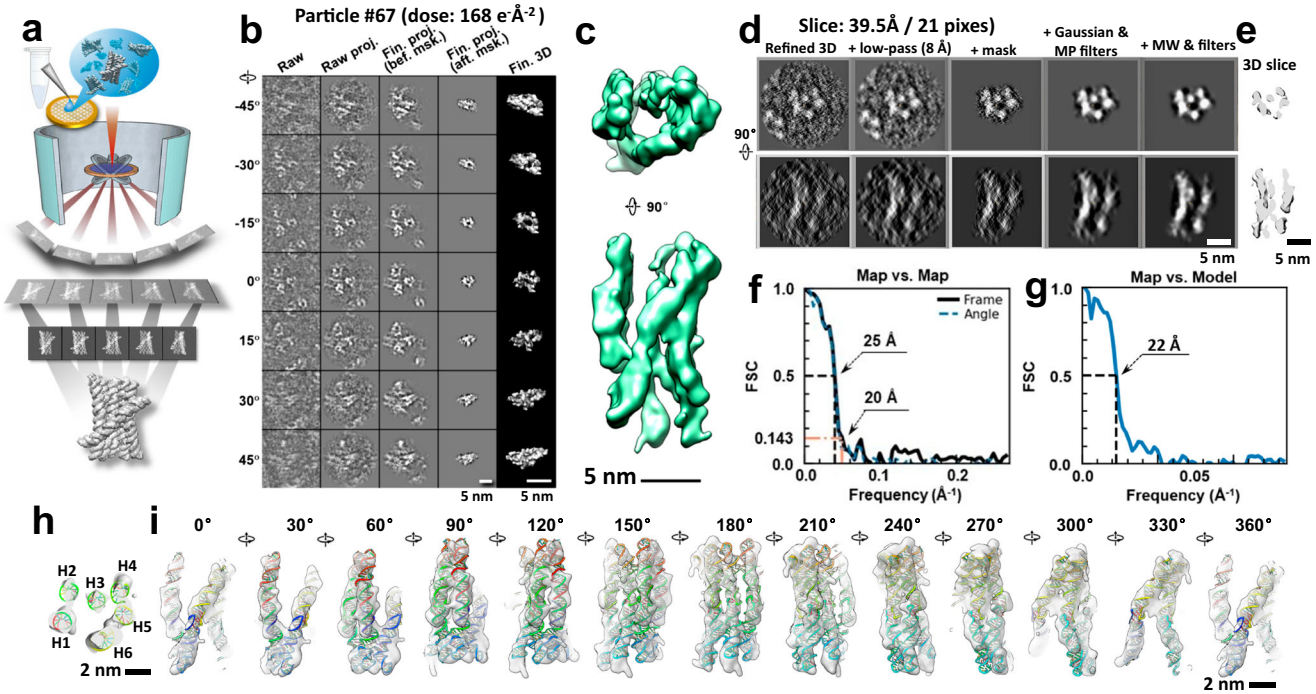

Fig. 3 | IPET 3D reconstruction and fitting model of an individual particle achieved at a dose of 168 e⁻Å⁻². **a** A schematic introducing the cryo-ET and 3D reconstruction methods. **b** The 3D reconstruction process of an individual particle by cryo-ET and IPET from a total electron dose of 168 e⁻Å⁻², displayed from seven represented tilting directions. **c** The final 3D map viewed from two perpendicular directions. **d** Central slices of 3D reconstruction intermediate viewed from two perpendicular directions, comparing the stages before and after the application of soft masks and noise reduction during 3D reconstruction, and after missing-wedge (MW) correction and low-pass filtering to 8 Å. **e** Central slices of the final 3D map generated from two perpendicular directions. **f** The resolution measured by FSC curves of two half-maps reconstructed using even-odd frames (solid line) and tilt angle (dashed line) at FSC = 0.5 and 0.143, respectively. **g** The resolution estimated by FSC curves computed between the final map and its fitting model-generated map at FSC = 0.5. **h** The fitting model in the map is demonstrated by its central cross-section. **i** The 3D map with the fitting model viewed from 12 directions (rotated every 30° along the vertical axis).

RNA origami 6HBC was computationally designed with specified base pairings to sequentially fold into secondary structures, such as stems, loops, and junctions (Supp. Fig. 1). These structures further condense into tertiary structures through the formation of pseudoknots, which involve kissing-loop (KL) interactions[33]. A study using small-angle X-ray scattering (SAXS)[33] demonstrated that 6HBC undergoes slow conformational changes over ~10 h after transcription ended, termed the maturation process (Fig. 1a). Meanwhile, cryo-EM SPA confirmed the structural heterogeneity of the sample and reconstructed two major conformations at subnanometer resolution: a "young" open conformation (PDB ID: 7PIK) and a "mature" closed conformation (PDB ID: 7PTL) (Fig. 1b)[33]. However, the conformations of most intermediates were challenging to identify or reconstruct (Supp. Fig. 2). Nonetheless, these observations led to the hypothesis of a transition process from the open conformation to a compact conformation, which involves the breaking and reforming of a central KL (Fig. 1b)[33].

In this study, we used cryo-ET and IPET to determine over a hundred tertiary structures of individual particles of 6HBC six hours after transcription ended. The statistical analyses of these tertiary structures reveal the spatial and orientational distributions of molecular inner helical connections, providing an opportunity to gain insights into the 6HBC self-folding landscapes and pathways during the maturation self-folding process.

Results

Cryo-EM image of individual RNA particles

To capture intermediates of the maturation process that happens after cotranscriptional folding, the 6HBC sample was vitrified ~6 hours after transcription finished[33]. Survey cryo-EM images of 6HBC particles embedded in vitreous ice revealed evenly distributed particles (Fig. 1c). Zoomed-in images of particles, consisting of 5–6 dots with a diameter of ~20 Å, appeared as "O", "C", or "L" shapes with diameters ranging from ~60–100 Å (Fig. 1d). Zoomed-in images of the fiber-shaped particles, with fibers measuring ~20 Å in width and ~150–200 Å in length, displayed irregular shapes (Fig. 1e); some appeared in parallel bundles, while others formed V-shaped bundles ranging from ~60–100 Å. The general shapes were consistent with those examined by optimized negative-staining (NS) EM (Fig. 1f–h). The observed dot- and fiber-type features aligned with the previously reported top and side views of the 6HBC[33]. The ~20 Å diameter of the dot and fiber, similar to that of an RNA helix, suggests that a single RNA helix may be directly visible in the cryo-EM image. The direct observation of a single helix within a particle provides a basis for tertiary structure determination from that particle. The coexistence of "O", "C", and "L" shapes in their top view and the coexistence of the parallel and crossing bundle shapes in their side view confirm the structural heterogeneity of 6HBC transcriptional products.

Assessment of electron-dose limit for RNA sample

Increasing the electron dose enhances the SNR in RNA images, thereby improving the resolution of 3D reconstructions. However, higher doses also lead to significant radiation damage, compromising the high-resolution details. Conversely, a lower electron dose minimizes radiation damage while preserving higher-resolution structural details but reduces SNR, leading to decreased resolution in 3D reconstructions due to increased noise. Therefore, achieving high-resolution images necessitates careful optimization of the electron dose to balance SNR with radiation damage. Although extensively studied[34], the optimal dose limit remains undefined, likely due to sample-dependent variability.

https://doi.org/10.1038/s41467-024-52914-1

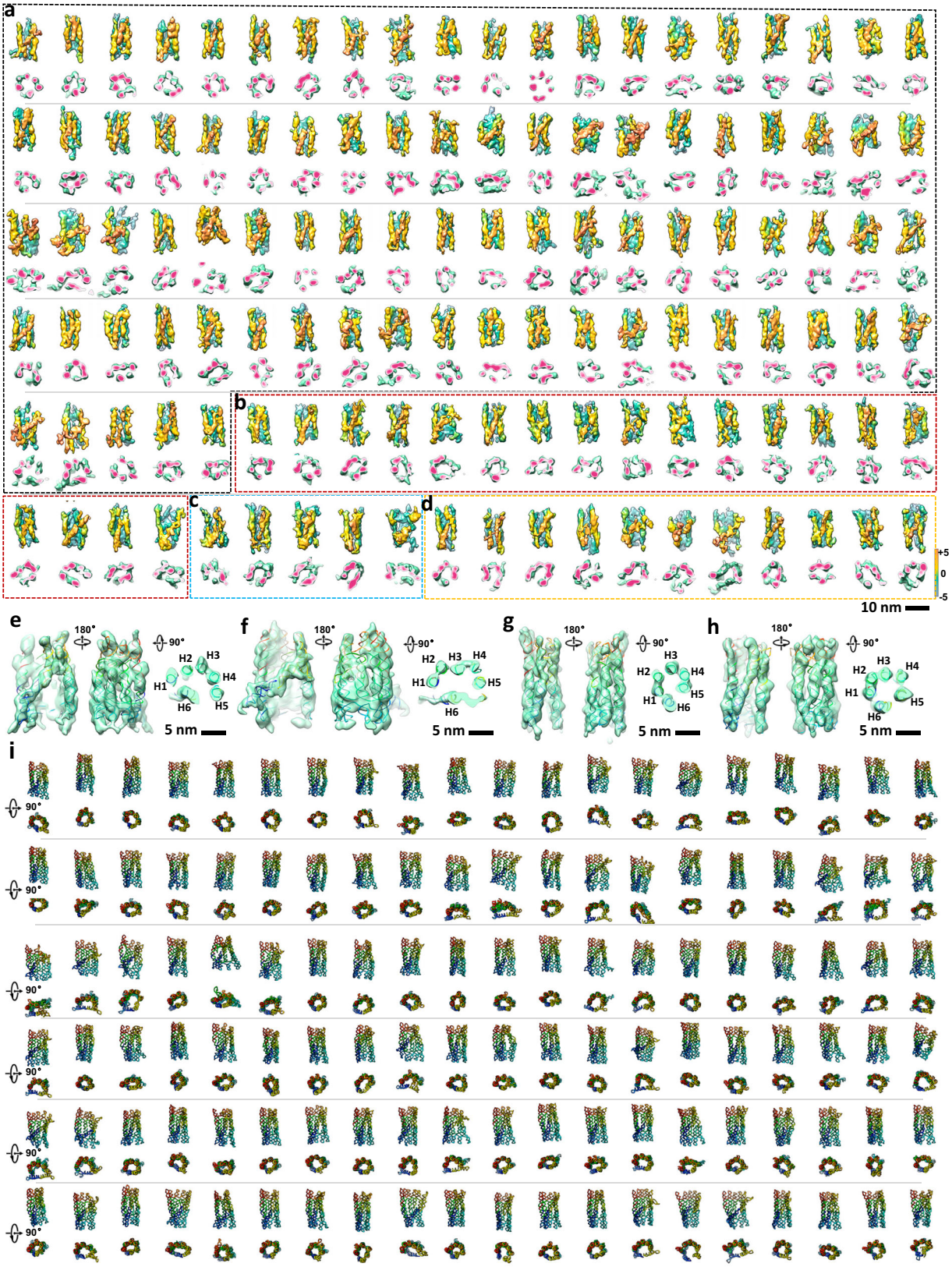

Fig. 4 | A gallery of 120 IPET 3D reconstructions and corresponding fitting models of RNA origami 6HBC. a A total of 85 IPET 3D density maps were reconstructed at a total electron dose of 168 $e^{-}Å^{-2}$. **b** Nineteen maps reconstructed at a dose of 120 $e^{-}Å^{-2}$. **c** Five maps reconstructed at a dose of 107 $e^{-}Å^{-2}$. **d** Eleven maps reconstructed at a dose of 54 $e^{-}Å^{-2}$. **e**, **f** Two representative young-like particles with their fitted models, displayed from three viewing directions. **g**, **h** Two representative mature-like particles with their fitted models, viewed from three directions. **i** The fitted models of the corresponding particles shown in (**a**–**d**) are displayed from two perpendicular views. The sequence order is color-coded in a rainbow pattern.

To evaluate the electron dose limit for our RNA sample, we acquired cryo-EM images of the same specimen area, maintaining a constant dose of 50 $e^-Å^{-2}$ per image across a series of 20 images (Fig. 2a). The first image reflects damage from a dose range of 0–50 $e^-Å^{-2}$, while the final image shows accumulated damage from a dose range of 950–1000 $e^-Å^{-2}$. Monitoring the same particles throughout this series indicated that the majority maintained their structural integrity at doses up to ~200 $e^-Å^{-2}$, with some withstanding doses as high as ~350 $e^-Å^{-2}$ (Fig. 2b) before gradually degrading with increasing doses.

Quantitative assessment of this degradation involved comparing the first image of 144 particles with subsequent images captured at higher doses using Fourier ring correlation (FRC) curves (Fig. 2c). At frequencies below ~22–40 Å—likely affected by non-linear changes in background intensity from radiation damage or shifts in particle centers due to ice deformation—the FRC curves demonstrated a sequential decrease in correlation beyond the frequencies above ~22 Å (Fig. 2c). The correlation at higher frequencies deteriorates more rapidly than at lower frequencies. For instance, structural details at 10 Å are retained after an accumulated dose of 100 $e^-Å^{-2}$, but consistent details degrade to 20 Å when the accumulated dose reaches ~350 $e^-Å^{-2}$ (Fig. 2d), suggesting that high-resolution features are more susceptible to electron dose damage than lower-resolution features. A similar pattern of dose-resolution degradation has also been observed in protein studies under a maximum dose of 100 $e^-Å^{-2}$ [35].

Although the dose tolerance of RNA samples appears significantly higher than that of protein[36–38], as indicated by recent analyses using cryo-EM[38], the results are also aligning with reports that electron diffraction spots from adenosine crystals fade ten times slower than those from valine crystals[39]. This resilience may be attributed to the presence of aromatic bases, the phosphate backbone[36,37], and the conjugated π orbitals in the adenosine ring, which enable RNA to absorb and redistribute energy from inelastically scattered electrons more effectively than the sigma bonds in proteins. Therefore, we hypothesize that the extended π-stacking between adjacent bases in RNA, particularly in our sample where RNA origami is double-stranded, further enhances RNA resilience to radiation damage.

Structure of an individual RNA particle without averaging

To determine the 3D structure of a single RNA particle without averaging, we captured a tilt series of images using cryo-ET (Fig. 3 and Supp. Fig. 3a), administering a total dose of 168 $e^-Å^{-2}$. An ab initio 3D reconstruction was achieved through iterative alignment of the tilt images of an individual particle using the IPET 3D reconstruction protocol (Fig. 3b–d and Supp. Video 1). The final resolution of 3D reconstruction is ~25 Å as assessed based on the frame map-map Fourier shell correlation (FSC) analysis at FSC = 0.5 (Fig. 3f), rather than the higher resolution typically assessed by the "gold standard" FSC = 0.143. Additionally, the impact of soft-masks on these evaluations was indistinguishable (Supp. Fig. 3b–d).

After low-pass filtering to 8 Å, along with Gaussian and median filtering processes, the 3D map showcased the particle, measuring ~170 × 100 × 100 Å, featuring six rod-shaped densities bundled together (Fig. 3c, d). Each rod was connected to nearby rods at one or both ends. Although the diameter of these rods, ~20 Å, matches that of an RNA double helix, this resolution is insufficient to determine the spatial orientation of the helices due to the lack of visualization of the major and minor grooves of RNA double helix. However, considering the observed interactions between the RNA helices, which indicate the locations of RNA crossover junctions linking the helices together (Fig. 3h, i), the spatial orientation of the helices can be inferred within each rod-shaped density through rigid-body docking and adjusting the tilting and shifting of each helix in the template model. A final fitting model was achieved by further refining the tilting of the four helical segments (the coaxially stacked helices of the 6HBC model) within each rod-shaped density, followed by refining the loops between segments using Phenix software[40].

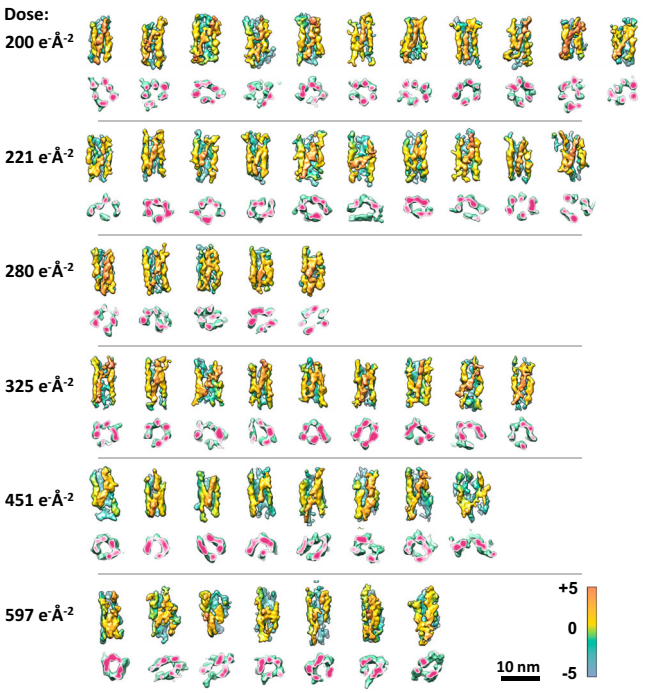

Fig. 5 | A gallery of 50 IPET 3D reconstructions of RNA origami 6HBC achieved at high doses in the range of 200–597 $e^-Å^{-2}$. Eleven reconstructions were achieved at a dose of 200 $e^-Å^{-2}$, ten reconstructions at a dose of 221 $e^-Å^{-2}$, five reconstructions at a dose of 280 $e^-Å^{-2}$, nine reconstructions at a dose of 325 $e^-Å^{-2}$, eight reconstructions at a dose of 451 $e^-Å^{-2}$, and seven reconstructions at a dose of 597 $e^-Å^{-2}$. The central cross-sections of the 50 IPET 3D reconstructions are shown below their corresponding maps.

Tertiary structures of a total of 170 RNA particles

By repeating the above IPET 3D reconstruction protocol, we reconstructed 3D density maps for 170 individual RNA particles from cryo-ET tilt series, acquired under a total dose ranging from 54 to 597 $e^-Å^{-2}$ (Figs. 4, 5). Examination of these 3D maps and their cross-sections consistently identified rod-shaped structures across all dose levels. However, the highest dose of 597 $e^-Å^{-2}$ compromised the fidelity of the fitting models, while the maps at the lowest dose of 54 $e^-Å^{-2}$ exhibited slight noisiness (Fig. 6a–d).

The resolutions for all 170 IPET maps were assessed using five different methods, as detailed in the Method section (Fig. 3f, g and Supp. Table 1). In brief, map-to-map FSC analyses based on both frame- and tilt-based half-data maps yielded comparable resolution ranges, 13 to 28 Å (mean ± sd: 21.3 ± 2.7 Å) and 18 to 29 Å (mean ± sd: 23.1 ± 1.8 Å), respectively, at FSC = 0.143 (Fig. 6e). However, these values seem to overestimate the resolution. At resolution beyond 20 Å, the major and minor grooves within each helix should be visible, as shown in the low-pass filtered PDB model and the SPA maps. However, none of the IPET maps could distinguish the major grooves, despite some of their resolutions being measured beyond 20 Å (Supp. Fig. 4). In contrast, utilizing the FSC = 0.5 criterion provided more conservative estimates, yielding resolutions from 23 to 35 Å (mean ± sd: 26.7 ± 2.1 Å) and 24 to 42 Å (mean ± sd: 27.9 ± 2.7 Å) for frame and tilt-based map-to-map FSC analyses, respectively (Fig. 6f). These resolutions align with those of 21 and 27 Å measured at FSC = 0.143 and 0.5, based on the FSC curve calculated between the reported 4.9 Å cryo-EM SPA map[33] and the IPET map of particle #72 (a particle similar to the SPA "mature" structure) (Supp. Fig. 5). Additionally, resolutions determined through map-to-

https://doi.org/10.1038/s41467-024-52914-1

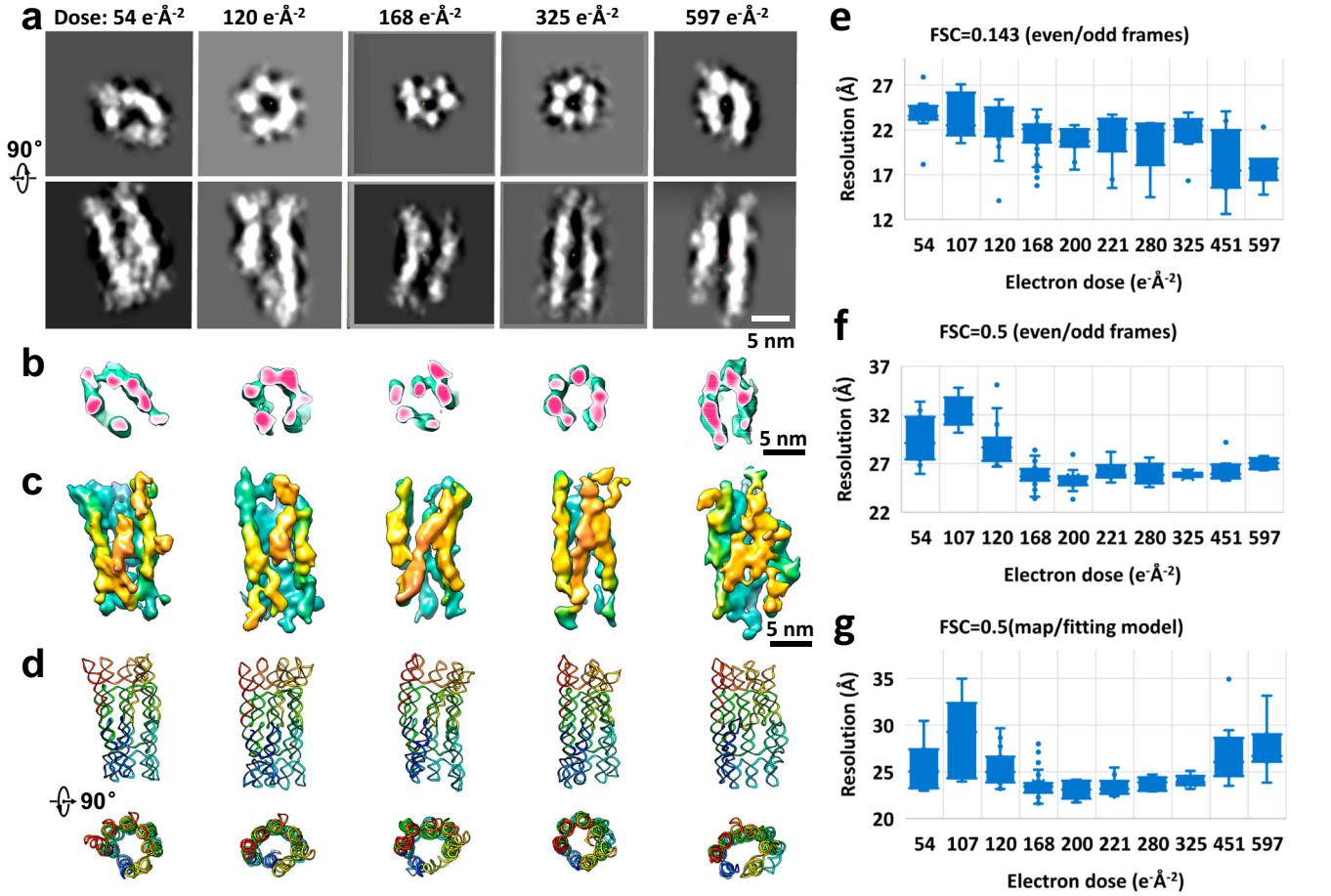

Fig. 6 | The effect of electron dose on IPET 3D reconstructions and their resolutions. a Examples of IPET 3D reconstructions achieved at various total electron doses ranging from 54 to 597 e$^-$Å^{-2}, with corresponding central slices shown (particles #10, 27, 67, 148, 165 from left to right panels). **b** The cross-sections of 3D reconstructions. **c** The 3D reconstructions. **d** The fitting models are viewed from two perpendicular directions, with rainbow-colored sequences indicating the order from the 5′ to 3′ end. **e**–**g** Plots of the resolutions of IPET 3D maps against their acquired electron doses. The resolutions are estimated by three different methods/criteria. The data for these plots is shown in Supp. Table 1.

model FSC analysis between the IPET map and its fitting model at FSC = 0.5 ranged from 22 to 35 Å (mean ± sd: 24.3 ± 2.2 Å) (Fig. 6g)[41], which slightly surpassed those assessed through the map-to-map FSC analyses at the same FSC. Despite these resolution variances, the analysis of structural features via low-pass filtering of the "mature" density map reconstructed from the SPA cryo-EM density map and its fitting PDB model (Supp. Fig. 4) indicated that, although major grooves were challenging to discern, a rod-shaped feature of helical density remained visible at resolutions of 20 and 25 Å (Supp. Fig. 4a, b). These features were also observed in the density maps and their cross-sections of the "mature-like" particles #67, #60, #40, and #82 (Supp. Fig. 4c), confirming the IPET resolution achieved at ~25 Å.

To optimize the imaging dose, we investigated how dose affects the 3D map resolution through the comparisons of their cross-sections and 3D maps with the fitting models (Fig. 6a–d), and statistically analyses of their resolutions achieved under each dose level (Fig. 6e–g). While the resolution distribution assessed using the map-to-map FSC = 0.143 criterion suggested improving resolution with an increase in dose (Fig. 6e), this finding was inconsistent with the known effect of radiation damage and with observations of radiation damage in 2D images (Fig. 2). In contrast, both the map-to-map and map-to-model FSC = 0.5 criteria depicted a U-shaped distribution against the dose (Fig. 6f, g), aligning with the logic that a lower dose results in lower resolution and a higher dose results in higher radiation damage and lower resolution. Thus, the resolution measured based on the map-to-map FSC = 0.143 criterion is not entirely accurate, leading to the decision to use only resolutions measured based on the FSC = 0.5 criteria as the final resolution.

The comparison of two resolution distributions estimated by FSC = 0.5 (Fig. 6f, g) showed the highest average resolution (~25.3 Å for map-to-map and ~23.1 Å for map-to-model) was achieved at a dose of 200 e$^-$Å^{-2}, with the second highest (~25.7 and 23.5 Å) occurring at a dose of 168 e$^-$Å^{-2}. Lower doses (ranging from 54 to 120 e$^-$Å^{-2}), and higher doses (ranging from 451 to 597 e$^-$Å^{-2}) resulted in decreased average resolutions, spanning from 28.7 to 31.6 Å (map-to-map) and 25.4 to 29.7 Å (map-to-model), respectively. These declining resolutions are attributable to increased SNR and accumulated damaged data, which hinder alignment accuracy and increase the percentage of inconsistent structural details. Analyses indicated that the optimal dose for achieving the highest resolution falls within the range of 120–325 e$^-$Å^{-2}.

This optimal dose range exceeds the commonly used dose for SPA studies of proteins at atomic resolution, even though a 3.5 Å resolution structure of ribosome was recently achieved under a dose range of 120–140 e$^-$Å^{-2} [4], which is significantly higher than the dose limit historically measured decades ago[42]. Despite reports that RNA exhibits greater resilience to radiation damage compared to proteins[36,37], doses exceeding 200 e$^-$Å^{-2} are rarely used in cryo-EM studies[42,43]. To avoid critiques and unnecessary arguments from experts on these rarely used doses, only the results achieved at doses no more than 168 e$^-$Å^{-2} were considered for further structural analysis. Consequently, our achieved average resolution ranged from 23.3 to 32.3 Å (Fig. 6f).

https://doi.org/10.1038/s41467-024-52914-1

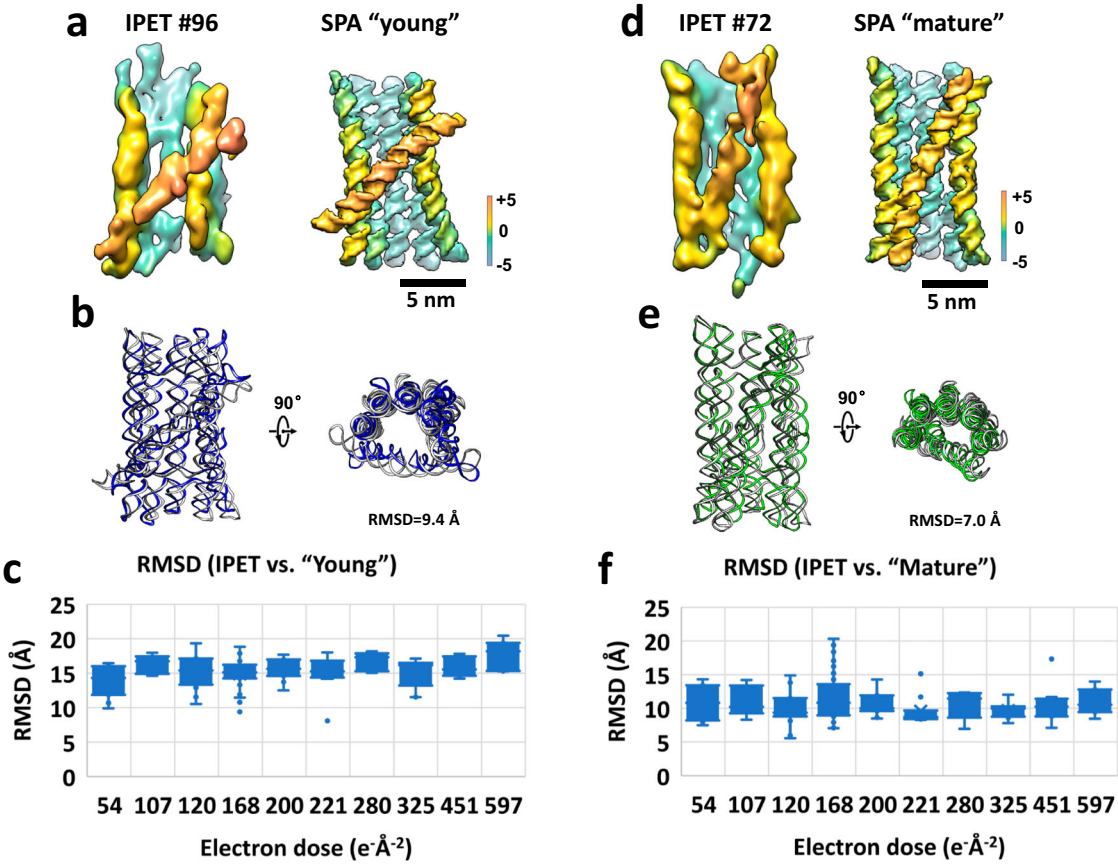

Fig. 7 | Representative IPET particles compared to two SPA structures. a The IPET representative structure (particle #96, obtained at a dose of 168 $e^-Å^{-2}$) with a conformation similar to the SPA "young" conformation (obtained at a dose of 60 $e^-Å^{-2}$)[33]. **b** The superimposed "young" and IPET structures viewed from two perpendicular directions, with an RMSD of 9.4 Å. **c** The box plot of the mean RMSDs against the "young" structure, distributed based on the achieved electron dose. **d** A similar comparison of the IPET structure (particle #72, obtained at a dose of 168 $e^-Å^{-2}$) and the SPA "mature" conformation (obtained at a dose of 60 $e^-Å^{-2}$)[33]. **e** The superimposed "mature" and IPET structures viewed from two perpendicular directions, with an RMSD of 7.0 Å. **f** The box plot of the mean RMSDs against the "mature" structure, distributed based on the achieved electron dose.

Validation of 3D reconstruction

It has long been speculated whether a structurally meaningful 3D reconstruction, including tertiary structure, could be achievable from a single particle without averaging[13]. To rigorously validate the tertiary structure achieved using IPET method, we employed the following five analytical approaches:

SPA reconstructions. We examined the same 6HBC sample under a dose of 60 $e^-Å^{-2}$ using the conventional cryo-EM SPA technique. This process resulted in two major conformations: a 5.2 Å resolution "young" structure and a 4.9 Å resolution "mature" structure[33]. Comparing these structures with IPET maps, some maps exhibited conformations similar to the "young" structure (PDB ID: 7PTK) (Figs. 4e, f, 7a, b), while others aligned with the "mature" structure (PDB ID: 7PTL) (Figs. 4g, h, 7d, e). For a detailed comparison, the IPET map from particle #72, acquired under a dose of 168 $e^-Å^{-2}$ (Fig. 7d, e), has a similar structure to the "mature" (Supp. Fig. 5a), except for ~1 nm shift of H5 toward the particle center, and slight bending of one distal end of H6 away from the map (as indicated by orange arrows in Supp. Fig. 5a). The root mean square deviation (RMSD) between these two structures was 7.0 Å (Supp. Fig. 5c), indicating that a similar conformation can be achieved with varying particle counts (thousands vs. one) and doses (60 vs. 168 $e^-Å^{-2}$). The rationale for retaining one decimal place, rather than using whole numbers for the RMSD value, is explained in the Methods section.

Dose-filtering method validation[35]. To evaluate whether the high-dose portion affects the 3D reconstruction, we removed the last four tilted images (corresponding to the highest tilt angles, ±50° and ±45°) from the tilt series of the particle #72, acquired under the dose of 168 $e^-Å^{-2}$. The new 3D reconstruction, corresponding to an acquired dose of 136 $e^-Å^{-2}$ (a similar dose has been used to achieve atomic resolution protein structures by cryo-ET via subvolume averaging[4]), showed the rod-shaped feature of helix nearly identical to the original map (Supp. Fig. 6). The FSC curve calculated between these two maps demonstrated a frequency at FSC = 0.5 beyond the Nyquist limit (Supp. Fig. 6c), indicating that excluding the high-dose portion did not significantly affect the determination of the tertiary structure under a dose of 168 $e^-Å^{-2}$. Similarly, the observation of that the high-dose portion did not significantly affect the determined structure of the protein at atomic resolution was also reported under a dose of 100 $e^-Å^{-2}$ [35].

Low-dose validation. To directly assess whether high dose affect the determination of tertiary structure, we repeated the cryo-ET experiment at doses lower than 168 $e^-Å^{-2}$, yielding an additional 35 density maps. These included 19 maps at a dose of 120 $e^-Å^{-2}$, five maps at a dose of 107 $e^-Å^{-2}$, and 11 maps at a dose of 54 $e^-Å^{-2}$ (Fig. 4b–d). The central cross-sections and 3D maps showed clearly discernible rod-like structures under all low-dose conditions (Fig. 4b–d), regardless of the use of soft-masks or filters (Fig. 6a and Supp. Fig. 7a–d). These

https://doi.org/10.1038/s41467-024-52914-1

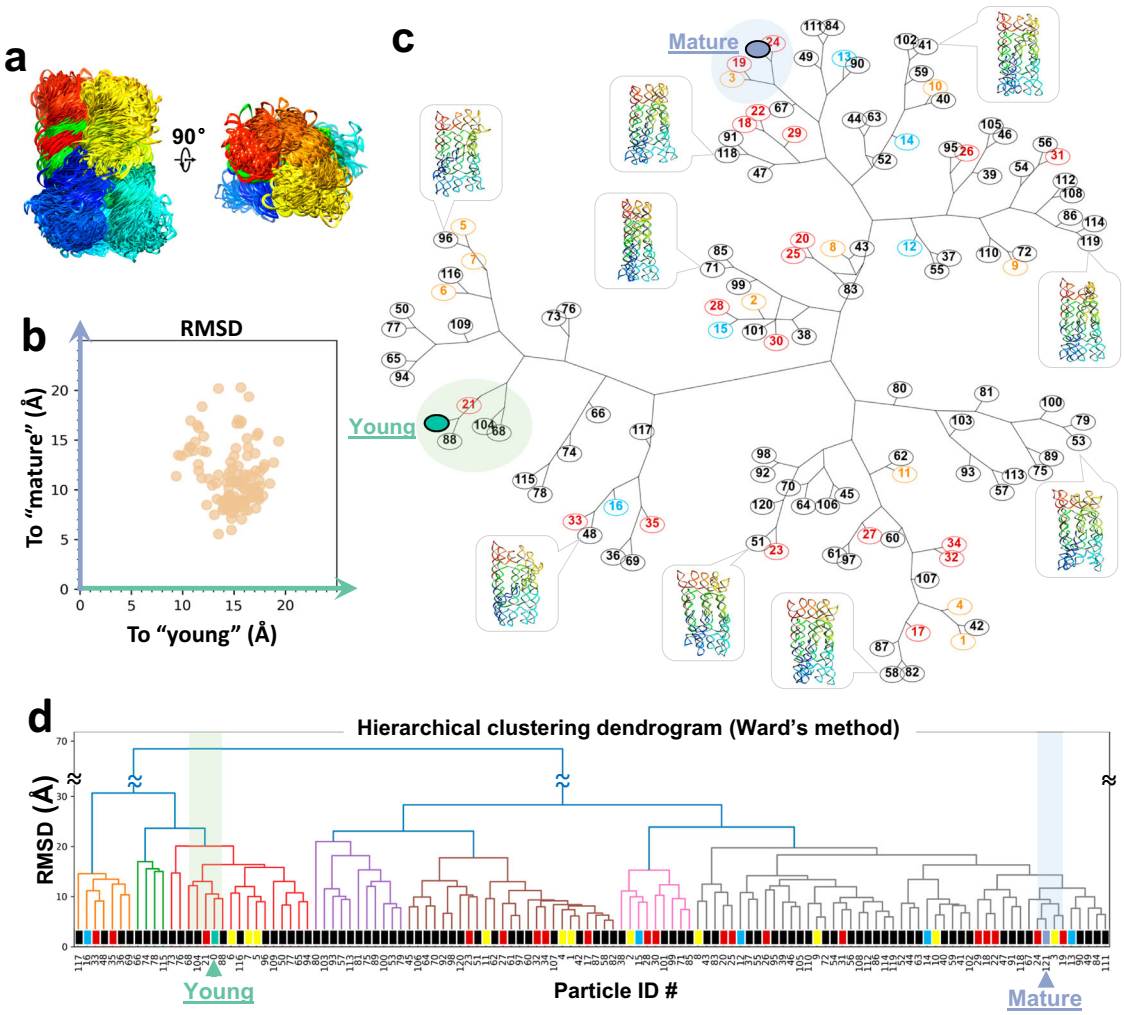

Fig. 8 | The distributions of 6HBC conformations. a Superimposition of 120 IPET structural models viewed from two perpendicular perspectives, with sequences color-coded in a rainbow gradient from the 5′ to 3′ end. **b** RMSD distribution of IPET structures in terms of they against the SPA structures of "young" (X-axis) and "mature" (Y-axis) conformations. **c** 2D hierarchical clustering tree diagram based on their RMSD values, using Ward's minimum variance method (see Methods section). The RMSD is calculated between each pair of structures, including the two SPA structures (PDB IDs: 7PTK and 7PTL, corresponding to "young" and "mature" conformations[33]) for comparison. The treemap illustrates the distances as the particle RMSD value relative to all others. Nine representative structures are shown alongside their corresponding indices. **d** 1D spectrum diagram from hierarchical clustering analysis of RMSD values. Structures obtained at a dose of 168 $e^{-}Å^{-2}$ are marked with black circles/rectangles (particles #36-120), those at 120 $e^{-}Å^{-2}$ in red (particles #17-35), at 107 $e^{-}Å^{-2}$ in cyan (particles #12–16), and at 54 $e^{-}Å^{-2}$ in yellow (particles #1–11). The "young" and "mature" conformations are labeled in "medium aquamarine" and "polo blue," respectively. Particles highlighted by green and blue disks/rectangle were used for local subtomogram averaging tests (detailed in the Methods section).

low-dose structures also resembled both "young" and "mature" conformations, further supporting the observation that these conformations are independent of the acquired doses (Fig. 7a–d).

RMSD analysis. RMSD values calculated for each IPET structure against the "young" and "mature" structures (Fig. 7c, f) showed an even distribution across different doses, indicating that the IPET structures are independent of the dose acquired. This finding is supported by the hierarchical distribution of the RMSDs among the IPET structures, which showed a random distribution across different doses (Fig. 8c, d).

IMOD software reconstruction[44]. To ascertain whether the helical features remains identifiable by third-party software, we reprocessed the cryo-ET tilt series acquired at doses of 168 $e^{-}Å^{-2}$, 120 $e^{-}Å^{-2}$, and 54 $e^{-}Å^{-2}$, respectively, using IMOD software. The central slices and their 3D reconstructions confirmed the visibility of rod-shaped structures across each particle, albeit with noisier reconstructions at the lower dose of 54 $e^{-}Å^{-2}$ (Supp. Fig. 8).

All the above validations provided evidence that the tertiary structure determined by the IPET method is likely not related to radiation damage.

Statistical analysis of structural variety

To analyze the detailed structural differences between the individual molecules, we measured distances and angles between the helices within each particle (Fig. 9). The distribution of the central cross-section area of the particle, defined by the centers of the six helices, ranged from ~1400 to ~3400 $Å^2$ (Fig. 9a), suggesting an average distance between two adjacent helices of ~23 to ~35 Å. The wide range of the helix distances indicates the coexistence of loose and compact conformation, with the compact structure being the lowest energy state as designed and studied by fitting SAXS curves[33].

Among the six helices, H6 exhibited the most extended distance to H1 and H5 and is the last helix to form the KL and join the helical bundle. Thus, H6's orientation relative to the other helices serves as one of the most sensitive parameters to detect the degree of

https://doi.org/10.1038/s41467-024-52914-1

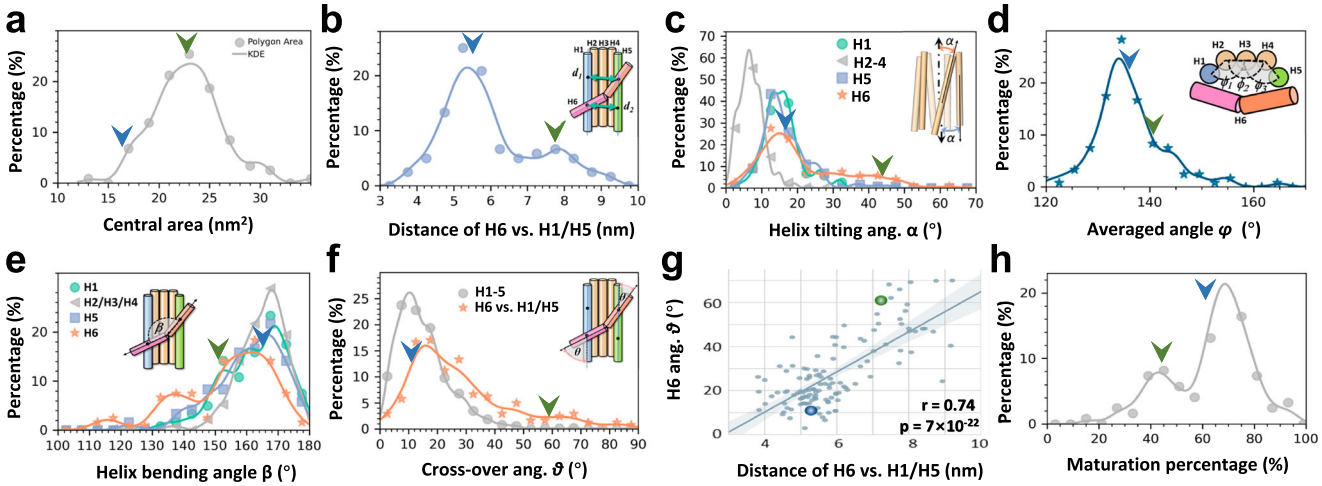

Fig. 9 | Statistical analyses of the internal structural variety. a A histogram of the helical bundle center area. **b** A histogram of the averaged distance $\bar{d}$ of H6 against the H1 and H5, as indicated by distances d_1 and d_2. **c** A histogram of the helix tilting angle α relative to the bundle center axis. **d.** A histogram of the helical bundle angle φ, formed within H1–5. **e** Characterization of the curvature of the H6 helix by the bending angle β between its two halves. **f** A histogram of the crossover angle θ of H6 relative to its connected H1 or H5, compared to the crossover angle formed among the remaining helices. **g** A correlation analysis of the H6 crossover angle θ against the averaged H6 distance, $\bar{d}$. **h** A histogram of the maturation percentage (MP, defined in the Method section). All measured data were fitted using kernel density estimation (KDE). The green and blue arrows/balls indicate the SPA determined "young" and "mature" conformations (PDB IDs: 7PTK and 7PTL), respectively[33].

maturation. The orientation of H6 is quantitively characterized by the averaged distance between H6 and H1/H5, denoted as $\bar{d}$, which is the averaged distances of d_1 (measured between the crossover points of H5/H6 and H1/H2) and the d_2 (measured by the crossover points of H1/H6 and H5/H4) (Fig. 9b). The distribution of $\bar{d}$ ranges from ~30 to ~100 Å with two major-population peaks at ~52 and ~79 Å. Notably, two SPA structures were located close to these major-population peaks, suggesting that they represent stable conformations in low-energy states[45].

By measuring the tilt angle of H6 against the bundle central axis by the angle α (Fig. 9c), the distribution showed a wider range of α (from 0° to ~60°) compared to the tilt angles of other helices (from ~0° to ~30°). The major peak of the angle α was distributed at ~15°, close to the ~17° tilting angle of H6 in the "mature" conformations[33], further confirming that "mature" is a low-energy state conformation. Additionally, H6 exhibits a broader, flatter distribution from ~30° to ~55°, covering the tilting angle, ~44° observed in the "young" conformations[33]. The histogram of angle α showed that the population, including the "mature" conformation, is substantially higher by ~6–10 times than that including the "young" conformation, indicating that most of the particles have successfully overcome the energy trap of KL in H6.

We then measured two curvatures within each particle: the helical bundle curvature and the H6 curvature. The helical bundle curvature, formed by H1–5, was measured by the average of three φ angles (Fig. 9d). The histogram shows a narrow range (~120° to 150°), except for a few φ values up to ~165°. The H6 curvature was measured by the bending angle β at the KL connecting the helix segments (Fig. 9e). The histogram showed two high-population peaks are at ~160° and ~135°, respectively, with the "young" and "mature" conformations sharing the highest peak population measured at angle β values of ~150° vs ~166°, respectively. The observed secondary peak reflects the existence of a secondary energy barrier other than the KL of H6.

By measuring the crossover angle θ at the crossover points of H6/H1 and H6/H5, the histogram showed a widely distributed range with the highest-population peak at ~17°, which covers the angle θ of the "mature" conformation, i.e., ~11°. However, the angle θ of the "young" conformation, i.e., ~59°, is located far from that of the "mature" conformations, suggesting the angle θ is a sensitive parameter to probe the folding process (Fig. 9f). The cross-correlation analysis of θ against the H6 distance $\bar{d}$ shows a reasonable high correlation, $r = 0.74$, suggesting that the tilting of H6 partially controls the distance between H1 and H5 (Fig. 9g).

The above analyses showed the distance $\bar{d}$, the H6 tilting angle α, and the H1–H5 bundle curvature angle φ are the three sensitive parameters that may be used to quantitively detect the folding process. Thus, we introduce a "maturation percentage" (MP) parameter to assess the level of folding by equally weighing these three parameters, followed by scaling to a percentage (see the definition and formula in Methods). The histogram of MPs shows that the 120 structures range from ~17% to ~95%, with two population peaks at ~45 and ~70% (Fig. 9h), in which the MPs of "young" and "mature" structures, i.e., ~47 and ~64%, respectively, are located close to each peak, confirming that those SPA-derived structures were located near the low-energy states.

Exploring the self-folding landscape

After transcription, RNA 6HBC particles undergo a 10-h maturation process. during which they experience large-scale, continuous conformational changes as part of a self-folding process. During this period, some RNA particles rapidly fold into their designed compact conformation, while others remain near their initial state due to local energy wells on their folding pathways. The cryo-EM SPA method has revealed two major conformations during this self-folding process. However, since SPA requires selecting a homogeneous population from all particles, the less common or unique conformations remain elusive. Under this consideration, we used the non-selection and non-averaged IPET maps to study the self-folding process.

The analysis of 120 unique structures obtained from individual particles confirms the presence of previously reported "mature" and "young" conformations, while also revealing many intermediate states, as well as highly compacted late-state and less-defined early-state conformations. The broad distribution of these conformation provides a detailed structural landscape of the molecular self-folding process, crucial for further understanding the RNA self-folding pathway and the mechanisms behind it. However, ordering and classifying these conformations is challenging due to the complexity of the 3D structures and their multidimensional flexibilities. Here we utilized the above-defined MP value as a simplified approach to sort the 120 structures

along a one-dimensional trajectory. According to this model, the closer a conformation is to the designed structure, the higher its MP value. Conversely, the farther it is from the designed structure, the lower its MP value.

Sorting these 120 structures based on their MP values helps us chronologically organize the primary conformational changes that occurred during the self-folding process (Fig. 10a–c). Sequentially morphing between the structures in the order of their MP values provides a visual pseudo-dynamic representation of molecular flexibility and the self-folding process (Supp. Video 1). For a 3D view of the folding landscape, MP values were plotted against two of their three parameters: the angles α and φ (due to the limited dimensions available for display), and then fitted to a curved surface. This 3D view represents a pseudo "free-energy" landscape[46] (Fig. 10b), exhibiting surface features including local hills and valleys, which suggest multiple folding pathways.

To zoom-in on a representative folding trajectory, seven particles with distinct conformations and evenly distributed MP values were selected and labeled on the MP 3D surface (Fig. 10a, b). For comparison, the "young" to "mature" conformations were also labeled (Fig. 10b). Along this trajectory, there is a significant increase in MP from the "young" to "mature" conformation, suggesting a major conformational change primarily due to the *α* angle of H6, while the helix angle *φ* remains relatively unchanged. This observation aligns with the reported mechanism in which H6 undergoes a breakage-reformation of the KL as it tilts to become parallel to the other helices during the transition from the "young" to "mature" conformations.

The overall conformational changes occurring along this representative trajectory can be interpreted as follows (Fig. 10a, c). At an MP of ~17%, helices H1–5 align parallel to form a plat bundle resembling a fence, with H6 positioned across the bundle surface, servicing as a belt. By increasing the MP to ~29%, the fence-edge helix, H5, tilts away from the fence surface plane towards H6, creating a gap between H6 and the fence plane, and forming an oval-shaped central cavity. As the MP further increases to ~37%, H5 tilts back and rejoins the H1–4 bundle, compressing the fence surface by bending it to a near-semicircle shape, resulting in an enlargement of the central cavity. When the MP reaches ~43%, H1–5 forms a complete semicircle locked by H6 interaction, resulting in the largest central cavity. This conformation is comparable to the "young" conformation[33]. As the MP increases to ~66%, the semicircle-shaped H1–5 buddle transforms into a near-circle-shaped bundle with "zig-zag" edges. This process reduced the central cavity, leaving the conformation similar to the "mature" conformation. The temporary dissociation of the KL of H6 was reported in this transition[33]. As the MP increases to ~80%, the central cavity further reduces as H6 joins the helix bundle by gradually aligning itself parallel to the other helices. At an MP of ~95%, all helices are nearly completely parallel and close to each other, indicating that the conformation has approached the designed structure and marking the culmination of the self-folding process. These landmark structures provide a brief overview of the dynamic self-folding process (Fig. 10c); however, the actual process is likely much more complex than described above.

Discussion

RNA molecules undergoing post-transcriptional self-folding and maturation display a broad range of structural diversity, as revealed by 3D structures determined from individual particles embedded in vitrified ice. This method avoids the use for selecting a homogeneous population from a pool of heterogeneous particles, averaging thousands of particles, or chemically fixing or staining the sample. We have managed to achieve an accurate single-particle 3D structure, in which its best resolution is approaching the theoretical limit[14]. Our achievements were facilitated by advanced cryo-EM equipment, a direct-detection camera, graphene oxide (GO) film, optimized electron doses, and large tilt steps. Determining the tertiary structure from individual particles of RNA provides an alternative method to explore the macromolecular structural dynamics and mechanism behind the self-folding process.

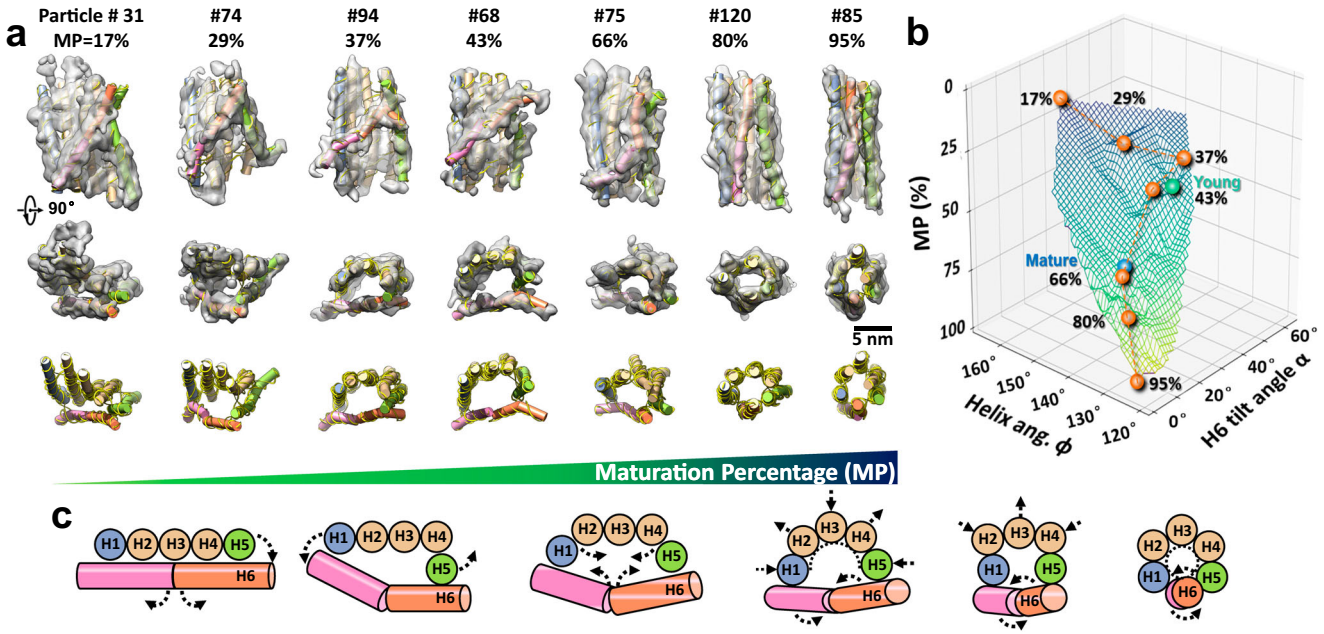

Fig. 10 | A hypothesis of the 6HBC maturation self-folding process. a Seven representative particles shown as 3D maps and tertiary models in the order of their maturation percentage (MP) values. The maps are displayed from two perpendicular directions with their fitting models, and the corresponding tertiary structures are shown in the bottom row. **b** A fitted curvy surface of the MP values distributed against bending angle α and φ. A possible self-folding pathway is illustrated by seven representative particles represented as orange spheres. The connections between conformations follow the order of their MP values, passing through the "young" and "mature" conformations, indicated by green and blue spheres, respectively. **c** Schematics of a self-folding landscape, depicting the maturation pathway/process of 6HBC from a "paddle with a stick"-shaped conformation to a "helix bundle"-shaped compact conformation through multiple steps of continuous conformational changes.

The statistical analysis of structural parameters in RNA origami has enabled the development of a unique metric for evaluating its self-folding or maturation process. IPET data provide detailed snapshots of the 3D structure of folding intermediates at the moment of sample freezing. An exceptional case is the 6HBC, wherein the kinetic latch of the H6 helix creates a kinetic trap that temporarily prevents the rest of the bundle (H1–H5) from assuming its optimal 120° 6-helix bundle configuration[33]. Despite this, forces from helix packing, driven by hydrogen bonds and stacking strain at the junctions, compress H6, inducing a kink at its midsection. This kink initiates the disengagement and restructuring of its KL by rotating 180° to allow the bundle to attain maturity[33]. Although the resolution of IPET is insufficient to directly visualize the rotation of the H6 segment, the observed bending or kink in H6, indicated by a secondary peak in the angle (orange line in Fig. 9e) at ~135°, indirectly supports the disengage-restructure or break-reform mechanism.

Additionally, the behavior observed in the bundle compaction process, as revealed through IPET data, manifests in two primary peaks. During this gradual transition process (approaching a state of equilibrium), these two discernible peak populations can be interpreted as representing an energy well between them (Fig. 9h), in accordance with the Boltzmann distribution in thermodynamics[45].

The self-folding process of RNA 6HBC[29] serves as a straightforward model for investigating the complex folding pathways of natural RNAs. This process helps elucidate these pathways and highlights the role of tertiary contacts. IPET data reveal significant diversity in the populations of "mature" and "young" states, with a transitional population of ~8% (around ten particles, as shown in Fig. 9h). This relatively uniform distribution suggests that the energy well is not particularly steep (Fig. 9h) and that KL breakage and formation occur through a continuous transition process. Conversely, the SPA structural variability analysis[33] (Supp. Fig. 2g) identified two distinct energy wells with steep sides, indicating limited conformational mobility and higher energy states for intermediates. The SPA model corresponds with expected dynamics, where base-pair interactions at the KL site break and reform, leading to highly stable states, during transitions between “young” and “mature” states, similar to kinetically trapped states observed in other RNA systems[47,48]. The discrepancy between IPET and SPA findings may be attributed to technical factors. The SPA process involves steps that exclude intermediate particle data (e.g., particle selection, 2D or 3D classification), potentially resulting in anomalies such as the blurring of the rotated helix in 2D class averages. Additionally, the relatively low population of intermediates can lead to insufficient data for reconstruction through averaging, along with near-equal occupancy of intermediate conformations, making them challenging to detect using maximum-likelihood methods during the conventional cryo-EM SPA analysis.

We propose that the IPET method can complement conventional SPA analysis by providing a global conformational diversity via the non-selecting and non-averaging structure determination of individual particles during dynamic biological processes. The biological processes include response to changes in time, temperature, pH, and polymerization reactions (such as folding during transcription, translation, and phase transition). The application of IPET to complex DNA-related nucleosome arrays, for example, has shed light on DNA conformational changes during assembly into distinct phases[49], which are driven by the compaction of inner- and intra-array interactions[50,51].

The IPET method can benefit from synergies with companion techniques such as time-resolved EM[52], chemical probing[53,54], and single-molecule FRET microscopy[55–57]. As the automation of IPET data acquisition and analysis advances, it will enable the creation of a comprehensive database of structural conformations for each macromolecular species. This database will be invaluable for machine learning methods designed to predict dynamic properties beyond the static structure of a macromolecule[58,59]. Such capabilities could lead to realistic predictions and the design of kinetics for biomolecular machines and self-assembly processes by acquiring time-resolved IPET data of multi-stage dynamic structures and complex folding pathways.

Methods

Transcription and purification of RNA origami

The RNA origami 6HBC sample was provided by Dr. Ebbe S. Andersen’s group[33]. In brief, synthetic DNA containing the T7 promoter, the 6HBC design, a 3’ BsaI linearization site, and flanking restriction enzyme sites for cloning was ordered from IDT in the form of a G-block, which was then cloned into a modified pUC vector. This plasmid was transformed into DH5-alpha cells and individual clones were sequence verified. Large-scale production of plasmid was performed using a MaxiPrep kit from Machery Nagel. The plasmid was subsequently linearized using BsaI (NEB), extracted three times with phenol-chloroform, and then ethanol precipitated. The linear plasmid was re-suspended in RNase-free water and diluted to 0.5 mg/mL.

Transcription reactions were setup in a buffer containing 40 mM Tris-Cl (pH 8.0) at 37 °C, 1 mM spermidine, 0.001% Triton X-100, 100 mM DTT, 12 mM $MgCl_2$, 8 mM NTP mix, and 0.05 mg ml^{-1} template DNA. Transcriptions were initiated upon the addition of in-house prepared T7 polymerase and carried out for 3 h at 37 °C. Precipitated inorganic pyrophosphate was pelleted by centrifugation at 17,000×*g* for 5 min at room temperature. The transcription reaction was then loaded onto a Superose 6 column (Cytiva) equilibrated with 25 mM HEPES buffer (pH 8.0), 50 mM KCl, and 5 mM $MgCl_2$. The major RNA peak was then collected and concentrated in 10-kDa-cutoff Amicon spin concentrators. The purified 6HBC was kept at room temperature for ~6 h before grid preparation for single particle analysis cryo-EM. Afterward, the sample was frozen to −20 °C for weeks before being shipped on dry ice to Berkeley for IPET analysis.

TEM specimen preparation by Cryo-ET and NS-EM

The sample was prepared for both cryo-EM and optimized negative-staining EM (OpNS-EM)[60,61]. Briefly, a 4 µl aliquot of the sample (diluted concentration: 0.3 mg/ml) was placed on a single layer graphene oxide support film on lacey carbon, 300 mesh copper grid (Ted Pella Inc., Redding, CA, USA) that had been glow-discharged for 15 s prior to cryo-EM specimen preparation. After blotting with filter paper from one side for 3.5 s, the grids were flash-frozen in liquid ethane at ~90% humidity and 4 °C with a Leica EM GP rapid-plunging device (Leica, Buffalo Grove, IL, USA) before being transferred into liquid nitrogen for storage. Meanwhile, OpNS-EM specimens were prepared as follows: a 4 µl aliquot of the sample (diluted concentration: 0.25 mg/ml) was placed on ultra-thin carbon film grids (CF-200-Cu-UL, Electron Microscopy Sciences, Hatfield, PA; Cu-200CN, Pacific Grid-Tech, San Francisco, CA USA) that had been glow-discharged for 15 s. After 1 min of incubation, the excess solution on the grid was removed by filter paper blotting. The grid was then washed with water and stained with 1% (w/v) uranyl formate (UF). The excess UF solution was removed by blotting the grid with filter paper from the opposite side of the carbon film before air-drying with nitrogen.

Cryo-EM and cryo-ET data acquisition

The cryo-EM specimens were imaged using a Titan Krios G2 and G3i TEM (Thermo Fisher Scientific) equipped with a Gatan energy filter (Gatan, Inc., Pleasanton, CA, USA) and operated at 300 keV. Micrographs were acquired using a Gatan K3 direct electron detector in correlated double sampling (CDS) mode[62] and super-resolution mode with a defocus of ~2 µm, controlled by SerialEM[63]. Un-tilted micrographs were acquired at a nominal magnification of 81 k× (corresponding to ~0.94 Å/pixel) with an exposure time of ~5.5 s (~0.11 s for each frame) and a dose rate of ~8 $e^{-}Å^{-2}s^{-1}$. The tilt series were acquired using a symmetric tilt scheme starting from 0° to the highest angle. The tilt series comprised three rounds of imaging sessions.

In the first round, acquired on a Krios G2 at 81 k× magnification (corresponding to ~0.94 Å/pixel) and a dose rate of ~8 $e^-Å^{-2}s^{-1}$, four tilt series were obtained in a tilting range of ±60° in a tilting step of 5° and total dose of ~325 $e^-Å^{-2}$ (at exposure time of ~1.43 s per tilt image); two series were collected in a tilting range of ±50° in a tilting step of 5° and a total dose of ~168 $e^-Å^{-2}$ (at an exposure time of ~0.88 s per tilt image); one series was obtained in a tilting range of ±51° in a tilting step of 3° and total dose of ~280 $e^-Å^{-2}$ (at an exposure time of ~0.88 s per tilt image); one series was acquired in a tilting range of ±60° in a tilting step of 5° and total dose of ~200 $e^-Å^{-2}$ (at an exposure time of ~0.88 s per tilt image); one series was collected in a tilting range of ±56° in a tilting step of 7° and total dose of ~221 $e^-Å^{-2}$ (at an exposure time of ~1.43 s per tilt image).

In the second round, acquired on a Krios G3i at a nominal magnification of 53 k× (corresponding to ~1.67 Å/pixel) and a dose rate of ~2.91 $e^-Å^{-2}s^{-1}$, one tilt series was obtained in a tilting range of ±50° in a tilting step of 5° and total dose ~54 $e^-Å^{-2}$ (at an exposure time of ~0.88 s per tilt image); one series was acquired in a tilting range of ±50° in a tilting step of 5° and total dose of ~107 $e^-Å^{-2}$ (at an exposure time of ~1.75 s per tilt image); one series was collected with a tilting range of ±50° in a tilting step of 5° and a total dose of ~451 $e^-Å^{-2}$ (at an exposure time of ~7.39 s per tilt image); one series was collected in a tilting range of ±50° in a tilting step of 5° and total dose of ~597 $e^-Å^{-2}$ (at exposure time of ~9.76 s per tilt image).

In the third round, acquired with a Krios G3i at a nominal magnification of 53 k× (corresponding to ~1.67 Å/pixel) and a dose rate of ~3.07 $e^-Å^{-2}s^{-1}$, two tilt series were collected with a tilting range of ±49° in a tilting step of 7° and a total dose of ~120 $e^-Å^{-2}$ (at exposure time of ~2.61 s per tilt image). The dose at 60° was 1.41 times higher than the dose at 0°, and the exposures were proportional to the inverse cosine of the tilt angle to the 1/2 power.

NS-EM data acquisition

The NS-EM specimens were examined using a Zeiss Libra 120 Plus TEM (Carl Zeiss NTS, Overkochen, Germany), equipped with a LaB_6 gun operating at 120 kV, an in-column energy filter, and a 4 k × 4 k Gatan UltraScan 4000 charge-coupled device (CCD) camera. The un-tilt micrographs were acquired at near Scherzer defocus and at a magnification of 80 k× (corresponding to 1.48 Å/pixel) with a dose of ~100 $e^-Å^{-2}$.

IPET image preprocessing

Motion correction of the multi-frame images from the K3 camera was conducted by MotionCor2[64]. The tilt series of whole micrographs were first aligned using IMOD[44]. The Contrast Transfer Function (CTF) was determined using the GCTF software package[65] and then corrected by TOMOCTF[66]. To reduce the image noise, tilt series were processed using an in-house developed machine learning software (manuscript in preparation), median-filter software, and a contrast enhancement method[21].

IPET 3D reconstruction

In the pipeline of IPET 3D reconstruction[19], a CTF-corrected tilt series containing a single or few RNA origami 6HBC particles was extracted from the full-sized tilt series. This allows us to perform "focused" 3D reconstruction, in which the reconstruction is less sensitive to image distortion, tilt-axis variation with respect to tilt angle, and tilt angle offset. Initially, each targeted 6HBC particle was windowed and extracted from the whole-micrograph tilt series into a small-size tilt series measuring ~256 × 256 pixels (1.88 Å/pixel) for the first round of data at 81 k× magnification, ~320 × 320 pixels (1.67 Å/pixel) for the second round of data at 53 k× magnification, or ~288 × 288 pixel (1.67 Å/pixel) for the third round of data at 53 k× magnification.

To start the 3D reconstruction, an ab initio 3D map was generated as an initial model by back-projecting the small-size tilt series. During the iteration and refinement processes, a set of Gaussian low-pass filters and soft-boundary circular and particle-shaped masks were automatically generated and sequentially applied to the tilt series and projections of the references to increase their signal-to-noise ratio (SNR). To reduce the missing-wedge artifact caused by the tilt limit, the final 3D maps were subjected to a low-tilt tomographic 3D reconstruction method (LoTToR)[19,20]. Finally, all IPET 3D reconstructions were low-pass filtered to 8 Å using EMAN software[67], followed by Gaussian filtering (the standard deviation is 3.0), median filter (3 × 3 × 3), and rendered in UCSF Chimera software[68].

Resolution analysis of the IPET map

The resolution of each 3D density map (Fig. 6e–g, and Supp. Table 1) was assessed using five different methods (details in method section). **(i) Frame-based map-to-map FSC analysis** (solid line in Fig. 3f): FSC curve was calculated between two 3D maps reconstructed from each of half-frames at each tilt angle (based on their odd and even index of frames), using IPET aligned particle tilt series[8]. The frequencies at which the FSC curve begins to fall below the values of 0.143[14] and 0.5[69,70] were used as estimated resolutions (Supp. Table 1). While better resolutions for all 170 maps were provided based on FSC = 0.143, ranging from 13 to 28 Å (mean ± sd.: 21.3 ± 2.7 Å), these values appear over-optimized as they do not allow distinction between the large and small grooves within each helix. A more conservative estimate using FSC = 0.5 yielded resolutions from 23 to 35 Å (mean ± sd.: 26.7 ± 2.1 Å). **(ii) Angle-based map-to-map FSC analysis** (dashed line in Fig. 3f)[41] FSC curves were calculated between two maps reconstructed from each of the half-tilt images (based on their odd and even index of tilt angles). The frequencies at FSC = 0.5 and 0.143, respectively, were used as the assessed resolutions. Results were similar to the frame-based analysis, with resolutions from 18 to 29 Å (mean ± sd.: 23.1 ± 1.8 Å) at FSC = 0.143, and from 24 to 42 Å (mean ± sd: 27.9 ± 2.7 Å) at FSC = 0.5 (Supp. Table 1). Again, the resolution based on FSC = 0.5 provides a more realistic assessment. **(iii) Map-to-model based FSC analysis** (Fig. 3g)[41] The FSC curve between the final IPET reconstruction and the map generated from its fitting model was computed, and the frequencies at FSC = 0.5 were used as the estimated resolution. The density map of the fitting model was generated by the *molmap* command in UCSF Chimera[68]. Assessed resolutions ranged from 22 Å to 35 Å (mean ± sd: 24.3 ± 2.2 Å) at an FSC = 0.5 threshold (Supp. Table 1). **(iv) SPA-based map-to-map FSC analysis** (Supp. Fig. 5b) FSC curve between the reported 4.9 Å cryo-EM SPA map[33] an IPET map of a particle #72 that has a similar conformation was calculated. The frequencies at FSC = 0.143 and 0.5 indicate the resolutions were 21 and 27 Å, respectively. **(v) Observable structural features** (Supp. Fig. 4) The visibility of structural features and their resolution were analyzed by low-pass filtering of a density map reconstructed from the SPA cryo-EM density map and its corresponding PDB model (Supp. Fig. 4a, b). This analysis confirmed that individual helices and large grooves are distinguishable at resolutions above 25 Å, but identifying these features becomes challenging at lower resolutions. Representative IPET maps (particles #67, #60, #40, and #82) demonstrated structures akin to the 'mature' conformation (Supp. Fig. 4c). While large grooves were difficult to discern, the helices remained visible (Supp. Fig. 4c). Cross-sectional views at resolutions of 20 and 25 Å showed helix contrast comparable to that observed in the SPA map and model (bottom panel in Supp. Fig. 4a–c), validating that IPET resolutions within the 20–25 Å range are achievable.

Validation of IPET structure

Like other techniques, the IPET approach has its own limitations in structure determination. It requires the macromolecule to exhibit low density and loose conformational, which poses challenges for transitional averaging methods. Structurally stable proteins, such as GroEL, Tobacco Mosaic Virus (TMV), and ferritin—typically used to validate

methods by traditional averaging—are not suitable for IPET due to the serious overlap of structural details in tilt images. This overlap complicates the distinction between details necessary for high-resolution reconstruction, resulting in final maps that display only globular overall shapes without detailed features, thereby limiting their biological applicability.

A suitable strategy to validate IPET involves using the same sample, such as 6HBC, in this study. Validation is achieved if the same structure can be reproduced using both IPET and traditional methods. This approach mirrors the early validation of nuclear magnetic resonance (NMR) structure by X-ray crystallography, where a structure identified among NMR-determined structures was similar to the crystal structure. Accordingly, we have previously validated the IPET method using the crystal and SPA structures[71] of 53 kDa cholesteryl ester transfer protein (CETP)[20]. Additionally, we employed third-party cryo-ET 3D reconstruction software, IMOD[44], for 3D reconstruction of the same macromolecules (Supp. Fig. 8). These include octahedral cage-shaped DNA origami particles embedded in vitrified ice, a 2D lattice[72], Y-shaped IgG antibodies[23,73,74], string-shaped DNA/RNA[25,33,51,75], floppy intermediate-density lipoprotein (IDL)[23] and very low-density lipoprotein (VLDL)[76], along with their interactions with antibodies.

Despite numerous validations, we routinely provide ground-truth images (raw data, first column in Fig. 3b) to substantiate any 3D reconstruction in both current and previous publications. These comprehensive approaches to validation not only demonstrate the IPET efficacy in capturing detailed structural information but also underscore its potential to complement existing structural determination methods by providing insights into conformational dynamics.

Structural modeling of individual 6HBC particle

The 6HBC RNA origami was designed using 720 bases[33], as shown in Supp. Fig. 1a. The corresponding secondary structure, including the high probability base pairs and single-stranded regions, was predicted using RNA structure software[77] (Supp. Fig. 1b). The blueprint of the design is presented in Supp. Fig. 1c. The PDB model (6HBC-mature[33]) was used as a template and rigid-body docked into the 120 IPET reconstructed 3D maps using Chimera[68]. This was followed by refining the position of each helix and its containing four helical segments. The loop structures were then repaired using Phenix software[40].

Validation of fitting modeling by RMSD analysis

The RMSD between the two models was evaluated after least-squares fitting using the *match* command in UCSF Chimera[57]. To evaluate the potential errors in the fitting process and their impact on the model, a blind test was conducted in which three individuals independently performed the fitting on the same map (i.e., particle #67 shown in Fig. 3). By aligning the three models, the RMSD values between each pair were calculated to be 3.4, 4.7, and 5.1 Å, respectively (Supp. Fig. 9a, b), indicating that the fitting error is considerably smaller than the structural variation among the particles, i.e., RMSD in range of ~5.3–25.4 Å.

Additional validation was performed by fitting a model to each of the two half-data maps reconstructed from the even and odd frames, respectively (Supp. Fig. 9c–e). The RMSD between these two half-data models was 3.2 Å, and the RMSD values of each half-data model against the full-data model were 4.3 and 5.1 Å, further confirming that the fitting error is considerably smaller than the minimal RMSD value among different particles (in range of ~5.3–25.4 Å).

While we used an established method—flexible fitting atomic structure (e.g., crystal, NMR, or AlphaFold2 structures) into low-resolution cryo-EM or SAXS map[78–80] to understand macromolecular dynamics—one might question why the RMSDs values are much lower than the resolution of the IPET maps. This is because RMSD and resolution refer to different concepts, even though they share the same unit and are often discussed together when analyzing structures. Resolution is a global measure of the overall map clarity, whereas RMSD focuses on specific structural regions or domains. In our case, the low-resolution rod-shaped density can be fitted more accurately than the overall resolution due to their cylinder shape and the observed conjunctions between helices, which constrain the docking positions and orientations of the helices. Additionally, the energy minimization used to refine the fitting model constrains the chemical bonds, limiting the flexibility of fitting helices at high resolution. This process produced RMSD values lower than the resolution of the experimental data, even though the data might not fully support such fine detail. In short, RMSD values being lower than the experimental resolution do not contradict the resolution; instead, they highlight the precision of the fitting in specific local regions of the structure.

In the RMSD analysis, we opted to use one decimal point for the RMSD values to present our results in a modest and practical way, rather than using whole numbers, as an expert has suggested due to the ~25 Å resolution of the IPET maps. RMSD is averaged from thousands of distances between atom pairs within aligned structures, so two to three decimal places are typically used, regardless of map resolution. Using whole numbers to compare the 120 IPET structures, which fall within a narrow RMSD range (5.3 to 25.4 Å), would result in significant overlap and loss of detail in the analysis.

Hierarchical clustering analysis of structural diversity

Hierarchical clustering analysis of RMSD values was performed using *scipy.cluster.hierarchy.linkage* in Python. The input is a list of the RMSD values between each of the two models from these 120 IPET models, 6HBC-young, and 6HBC-mature models[33]. The distance between the newly formed cluster u and each v was calculated using the 'ward' method[81], which employs the Ward variance minimization algorithm. The new entry $d(u,v)$ is computed as follows,

$$d(u,v)=\sqrt{\frac{|v|+|s|}{T}d(v,s)^2+\frac{|v|+|t|}{T}d(v,t)^2-\frac{|v|}{T}d(s,t)^2} \quad (1)$$

where u is the newly joined cluster consisting of clusters s and t, v is an unused cluster in the forest, $T=|v|+|s|+|t|$. The dendrogram and 2D tree diagram were plotted by the hierarchical clustering analysis of RMSD values.

Statistical analysis of structural diversity

Each helix of 6HBC-mature was divided into four short helices based on the positions of KL and crossover. The orientations of a total of 24 short helices in each particle were defined by 24 vectors, which were measured using DSSR software[82]. These vectors were then used for statistical analysis of the particle structural variety. For tilting angle measurement, the tilting angle of each helix was defined by averaging its two central vectors. Crossover angles were measured by two averaged vectors, each representing half of the helix containing two short helices. The helix curvature angle was measured by the angles between two averaged vectors within each half of the helix. The bending angle was measured by the two conjunctive vectors at the KL. The coupling angle was measured by two vectors within each half of the helix. The corresponding histograms were plotted and fitted with kernel density estimation in Python.

Maturation percentage (MP) definition

The MP was determined by averaging the contribution of these three parameters (the distance between H1–H5, the H6 tilting angle α, and the H1–H5 bundle curvature angle φ. This was expressed as a percentage, i.e.,

$$MP_i=\left\{1-\frac{1}{3}\times\left[\left(\frac{d_i-d_{\min}}{d_{\max}-d_{\min}}\right)+\left(\frac{\alpha_i-\alpha_{\min}}{\alpha_{\max}-\alpha_{\min}}\right)+\left(\frac{\varphi_i-\varphi_{\min}}{\varphi_{\max}-\varphi_{\min}}\right)\right]\right\}\times 100\% \quad (2)$$

Cryo-EM sample preparation for single particle averaging analysis

The cryo-EM study of the same sample has been reported in ref. 33, in brief, a Leica GP2 was prepared with the sample application chamber set to 100% humidity and 21 °C. The Leica GP2 was set with a manually calibrated blotting distance onto two Whatman no. 1 filter paper layers with a 4-s delay after sample application, followed by 6-s blotting time and then directly plunging into liquid ethane at −184 °C. ProtoChips Au-FLAT 1.2/1.3 300 mesh grids were glow-discharged for 45 seconds at 15 mA in a PELCA easiGlow immediately before sample application.

Single particle averaging analysis cryo-EM data collection

Data were acquired on a Titan Krios G1 equipped with a Cs corrector and a K2 camera (Gatan/Ametek), under a defocus range of −0.5 to −2.0 µm with a targeted dose of 60 $e^{-}Å^{-2}$ and a pixel size of 0.860 Å px^{-1}. Automated data collection was performed using EPU, and data saved as MRC files as reported in ref. 33.

Single particle averaging analysis data processing

All SPA analysis[33] was performed in cryoSPARC, with the preprocessing occurring in cryoSPARC V2 and the final refinements and 3D variability analysis in cryoSPARC V4[83]. Patch motion correction was performed with Fourier cropping by ½ and otherwise default settings. Patch CTF was used with default parameters for CTF correction. Micrographs were curated to remove bad ice, and micrographs with CTF fit worse than 10 Å, leaving 2393 curated exposures.

Particles were picked with a pre-trained Topaz[84] model (ResNet16, 64 units, with a downsampling factor of 4). The particle images were extracted with a box size of 256 pixels (430 Å) and downsized to 128 pixels, resulting in 264,890 particles. The 2D classification was performed with 100 classes and a circular mask with a diameter of 200 Å. Twenty-five Junk classes were excluded from further analysis, leaving 201,745 particles in the working stack. A four-class ab initio reconstruction was performed using 40k random particles, followed by heterogeneous refinement using all 4 volumes and all 201,745 particles. This resulted in two distinct classes, each resembling a six-helix bundle, with 69,577 and 69,948 particles, respectively.

These particles were re-extracted (256px box) and re-centered based on aligned shifts. Further refinement of these classes revealed some duplicate picks, which were then removed from the stack, leaving 113,076 particles.

To explore the possibility of further sub-populations of alternate conformers, we performed 3D variability analysis[9] using a mask that was low-pass filtered to 50 Å, dilated five voxels with a threshold set to 0.5 and soft-padded with a width of 15 voxels. 3DVA was performed, solving for three modes of variability, one of which appears to resemble real differences in the data, while the other two seem to contain noise. We then isolated particles along the reaction coordinate that showed the transition from conformer 1 to conformer 2 and made independent reconstructions from these intermediary particle stacks.

To further explore the possibility of additional sub-populations of conformers, we performed 3D classification without alignment into 2, 5, and 10 classes using standard parameters.

Averaging analysis of non-averaged IPET maps

Subtomogram averaging[85] has become a widely used method for achieving high-resolution 3D reconstructions from cryo-ET data. In this approach, subvolumes containing individual macromolecular particles are extracted from low-resolution 3D tomograms, which are reconstructed from large areas or entire micrographs. These subvolumes, consisting of a homogeneous population of particles, are then selected, aligned, and averaged into a 3D map to reduce noise in the reconstruction. While this method can achieve atomic resolution for some proteins[4], it remains challenging for many flexible macromolecules that undergo large-scale, continuous conformational changes, often resulting in only low to intermediate resolution.

To evaluate whether the averaging process could improve map resolution in our case, we selected particles that closely resembled the SPA "young" structures and averaged them into a single map. A similar approach was applied to the SPA "mature" structures. Specifically, four young-like particles (#21, #68, #88, and #104), which were closest to the SPA young structure based on their RMSD values relative to the SPA structures (shown in the green-disc shaded area of Fig. 8c), were selected, aligned, and averaged into a map (Supp. Fig. 10a) using Chimera software[68]. Similarly, three mature-like particles (#3, #19, and #24), which were closest to the SPA mature structure (shown in the blue-disc shaded area of Fig. 8c), were aligned and averaged following the same protocol (Supp. Fig. 10d).

Although the averaged maps showed some reduction in noise and retained structural details, such as rod-like helical densities, direct docking of the SPA structures into their corresponding averages revealed that some helices were misaligned compared to the references (as indicated by arrows in Supp. Fig. 10a, d). The FSC curves between the averaged maps and their corresponding SPA structures, at FSC = 0.5, indicated resolutions of 36-37 Å (last panel in Supp. Fig. 10a, d), which are comparable to the lowest resolution of the IPET map against their fitting model (Fig. 6g). This suggests that the averaged maps did not significantly improve resolution compared to the non-averaged maps.

Further analysis using flexible fitting of the ternary structures from the averaged maps showed, through FSC analysis, that the resolutions of the averaged maps against their newly fitted models were both at 23 Å (Supp. Fig. 10b, e). This resolution is similar to the typical resolution of the IPET maps against their fitting models under optimized doses (Fig. 6g). The RMSD values between the fitting models and their corresponding SPA structures were both 7.0 Å (Supp. Fig. 10c, f). However, FSC analysis between the fitting models and their corresponding SPA structures showed resolutions of 33–34 Å at FSC = 0.5, confirming structural differences between the models and their SPA counterparts (Supp. Fig. 10c, f).

This analysis suggests that while averaging can reduce noise, it does not improve the resolution beyond what can be achieved by non-averaged maps. However, we do not exclude the possibility that the limited number of particles averaged here may have restricted any potential resolution improvements. Whether the averaged structure represents a truly existing particle in reality remains unresolved, and further evaluation with a larger number of non-averaged structures at higher resolution is warranted.

Reporting summary

Further information on research design is available in the Nature Portfolio Reporting Summary linked to this article.

Data availability

The data supporting the findings of this study are available from the corresponding authors upon request. The sequence of RNA origami 6HBC is provided in Supp. Fig. 1. The 3D density maps of a total of 170 cryo-ET IPET 3D reconstructed particles of 6HBC produced in this study have been deposited in the EMDB under the following accession codes: EMD-25230 to EMD-25261, EMD-25270 to EMD-25357, EMD-40353, andEMD-40356 to EMD-40404. The associated cryo-ET raw images, tilt series, final 3D maps, fitting models, EMDB reports, and figure-related test maps have been uploaded to the Zenodo.org repository at: https://doi.org/10.5281/zenodo.13328107. The processes of IPET 3D reconstruction, including seven representatives of raw tilted images, projections of the intermediates, final reconstructions, and their fitting models shown at the corresponding tilted angles, are provided in the Supp. Figs. 11–180. The major steps of the image

processing, intermediates, the flexible fitting process, and the comparison of the fitting models, are presented in Supp. video 1. The related experimental parameters, inducing doses, camera types, tilt range, resolutions, and RMSDs of each particle, are provided in Supp. Table 1. All measured data used for producing the curves in figures are available in the Source Data file, which is provided with this paper. Source data are provided with this paper.

References

1. Li, X. et al. Electron counting and beam-induced motion correction enable near-atomic-resolution single-particle cryo-EM. *Nat. Methods* **10**, 584–590 (2013).
2. Yip, K.M. et al. Atomic-resolution protein structure determination by cryo-EM. *Nature* **587**, 157–161 (2020).
3. Hryc, C. F., Chen, D. H. & Chiu, W. Near-atomic-resolution cryo-EM for molecular virology. *Curr. Opin. Virol.* **1**, 110–117 (2011).
4. Xue, L. et al. Visualizing translation dynamics at atomic detail inside a bacterial cell. *Nature* **610**, 205–211 (2022).
5. Nakane, T. et al. Single-particle cryo-EM at atomic resolution. *Nature* **587**, 152–156 (2020).
6. Vilas, J. L., Tagare, H. D., Vargas, J., Carazo, J. M. & Sorzano, C. O. S. Measuring local-directional resolution and local anisotropy in cryo-EM maps. *Nat. Commun.* **11**, 55 (2020).
7. Liao, M., Cao, E., Julius, D. & Cheng, Y. Structure of the TRPV1 ion channel determined by electron cryo-microscopy. *Nature* **504**, 107–112 (2013).
8. Zhong, E. D., Bepler, T., Berger, B. & Davis, J. H. CryoDRGN: reconstruction of heterogeneous cryo-EM structures using neural networks. *Nat. Methods* **18**, 176–185 (2021).
9. Punjani, A. & Fleet, D. J. 3D variability analysis: resolving continuous flexibility and discrete heterogeneity from single particle cryo-EM. *J. Struct. Biol.* **213**, 107702 (2021).
10. Punjani, A. & Fleet, D. 3D flexible refinement: structure and motion of flexible proteins from cryo-EM. *Microsc. Microanal.* **28**, 1218–1218, (2022).
11. Jerkovic, I. & Cavalli, G. Understanding 3D genome organization by multidisciplinary methods. *Nat. Rev. Mol. Cell Biol.* **22**, 511–528 (2021).
12. van der Lee, R. et al. Classification of intrinsically disordered regions and proteins. *Chem. Rev.* **114**, 6589–6631 (2014).
13. Frank, J. *Electron Tomography* (Springer-Verlag, 2008).
14. Rosenthal, P. B. & Henderson, R. Optimal determination of particle orientation, absolute hand, and contrast loss in single-particle electron cryomicroscopy. *J. Mol. Biol.* **333**, 721–745 (2003).
15. Milne, J. L. & Subramaniam, S. Cryo-electron tomography of bacteria: progress, challenges and future prospects. *Nat. Rev. Microbiol.* **7**, 666–675 (2009).
16. Marx, V. Calling cell biologists to try cryo-ET. *Nat. Methods* **15**, 575–578 (2018).
17. Henderson, R. Realizing the potential of electron cryo-microscopy. *Q Rev. Biophys.* **37**, 3–13 (2004).
18. Grimm, R. et al. Electron tomography of ice-embedded prokaryotic cells. *Biophys. J.* **74**, 1031–1042 (1998).
19. Zhang, L. & Ren, G. IPET and FETR: experimental approach for studying molecular structure dynamics by cryo-electron tomography of a single-molecule structure. *PLoS ONE* **7**, e30249 (2012).
20. Zhai, X. et al. LoTToR: an algorithm for missing-wedge correction of the low-tilt tomographic 3D reconstruction of a single-molecule structure. *Sci. Rep.* **10**, 10489 (2020).
21. Wu, H. et al. An algorithm for enhancing the image contrast of electron tomography. *Sci. Rep.* **8**, 16711 (2018).
22. Liu, J. et al. Fully mechanically controlled automated electron microscopic tomography. *Sci. Rep.* **6**, 29231 (2016).
23. Lei, D. et al. Single-molecule 3D imaging of human plasma intermediate-density lipoproteins reveals a polyhedral structure. *Biochim. Biophys. Acta Mol. Cell Biol. Lipids* **1864**, 260–270 (2019).
24. Yu, Y. D. et al. Polyhedral 3D structure of human plasma very low density lipoproteins by individual particle cryo-electron tomography. *J. Lipid Res.* **57**, 1879–1888 (2016).
25. Lei, D. et al. Three-dimensional structural dynamics of DNA origami Bennett linkages using individual-particle electron tomography. *Nat. Commun.* **9**, 592 (2018).
26. Wang, S.-T. et al. Designed and biologically active protein lattices. *Nat. Commun.* **12**, 3702 (2021).
27. Rothemund, P. W. Folding DNA to create nanoscale shapes and patterns. *Nature* **440**, 297–302 (2006).
28. Geary, C., Grossi, G., McRae, E. K. S., Rothemund, P. W. K. & Andersen, E. S. RNA origami design tools enable cotranscriptional folding of kilobase-sized nanoscaffolds. *Nat. Chem.* **13**, 549–558 (2021).
29. Geary, C., Rothemund, P. W. & Andersen, E. S. A single-stranded architecture for cotranscriptional folding of RNA nanostructures. *Science* **345**, 799–804 (2014).
30. Bushhouse, D. Z., Choi, E. K., Hertz, L. M. & Lucks, J. B. How does RNA fold dynamically? *J. Mol. Biol.* **434**, 167665 (2022).
31. Lai, D., Proctor, J. R. & Meyer, I. M. On the importance of cotranscriptional RNA structure formation. *RNA* **19**, 1461–1473 (2013).
32. Woodson, S. A., Panja, S. & Santiago-Frangos, A. Proteins that chaperone RNA regulation. *Microbiol. Spectr.* https://doi.org/10.1128/microbiolspec.RWR-0026–2018 (2018).
33. McRae, E. K. S. et al. Structure, folding and flexibility of co-transcriptional RNA origami. *Nat. Nanotechnol.* **18**, 808–817 (2023).
34. Henderson, R. & Unwin, P. N. Three-dimensional model of purple membrane obtained by electron microscopy. *Nature* **257**, 28–32 (1975).
35. Grant, T. & Grigorieff, N. Measuring the optimal exposure for single particle cryo-EM using a 2.6 A reconstruction of rotavirus VP6. *Elife* **4**, e06980 (2015).
36. Fujiyoshi, Y., Uyeda, N., Morikawa, K. & Yamagishi, H. Electron microscopy of tRNA crystals. II. 4 A resolution diffraction pattern and substantial stability to radiation damage. *J. Mol. Biol.* **172**, 347–354 (1984).
37. Bury, C. S. et al. RNA protects a nucleoprotein complex against radiation damage. *Acta Crystallogr. D. Struct. Biol.* **72**, 648–657 (2016).
38. Ma, H., Jia, X., Zhang, K. & Su, Z. Cryo-EM advances in RNA structure determination. *Signal Transduct. Target Ther.* **7**, 58 (2022).
39. Glaeser, R. M. Limitations to significant information in biological electron microscopy as a result of radiation damage. *J. Ultrastruct. Res.* **36**, 466–482 (1971).
40. Liebschner, D. et al. Macromolecular structure determination using X-rays, neutrons and electrons: recent developments in Phenix. *Acta Crystallogr. D. Struct. Biol.* **75**, 861–877 (2019).
41. Lawson, C. L. et al. Cryo-EM model validation recommendations based on outcomes of the 2019 EMDataResource challenge. *Nat. Methods* **18**, 156–164 (2021).
42. Xue, H., Zhang, M., Liu, J., Wang, J. & Ren, G. Cryo-electron tomography related radiation-damage parameters for individual-molecule 3D structure determination. *Front. Chem.* **10**, 889203 (2022).
43. Kudryashev, M., Castano-Diez, D. & Stahlberg, H. Limiting factors in single particle cryo electron tomography. *Comput. Struct. Biotechnol. J.* **1**, e201207002 (2012).
44. Kremer, J. R., Mastronarde, D. N. & McIntosh, J. R. Computer visualization of three-dimensional image data using IMOD. *J. Struct. Biol.* **116**, 71–76 (1996).
45. Kuriyan, J., Konforti, B. & Wemmer, D. Chapter 8: The Boltzmann Distribution. In *The Molecules of Life: Physical and Chemical Prin-*

ciples (eds Kuriyan, J., Konforti, B. & Wemmer, D.) (Garland Science, Taylor & Francis Group, 2013) https://www.taylorfrancis.com/chapters/mono/10.1201/9780429258787-15/linking-energy-entropy-boltzmann-distribution-john-kuriyan-boyana-konforti-david-wemmer?context=ubx&refId=37ddf3e3-4e8a-4d44-8c86-6dd2ecc9e9ea.
46. Dinner, A. R., Sali, A., Smith, L. J., Dobson, C. M. & Karplus, M. Understanding protein folding via free-energy surfaces from theory and experiment. *Trends Biochem. Sci.* **25**, 331–339 (2000).
47. Li, S. et al. Topological crossing in the misfolded Tetrahymena ribozyme resolved by cryo-EM. *Proc. Natl Acad. Sci. USA* **119**, e2209146119 (2022).
48. Bonilla, S. L., Vicens, Q. & Kieft, J. S. Cryo-EM reveals an entangled kinetic trap in the folding of a catalytic RNA. *Sci. Adv.* **8**, eabq4144 (2022).
49. Woodson, S. A. Compact intermediates in RNA folding. *Annu. Rev. Biophys.* **39**, 61–77 (2010).
50. Zhang, M. et al. Angle between DNA linker and nucleosome core particle regulates array compaction by individual-particle cryo-electron tomography. *Nat. Commun.* **15**, 4395 (2024).
51. Zhang, M. et al. Molecular organization of the early stages of nucleosome phase separation visualized by cryo-electron tomography. *Mol. Cell* **82**, 3000–3014.e3009 (2022).
52. Frank, J. Time-resolved cryo-electron microscopy: recent progress. *J. Struct. Biol.* **200**, 303–306 (2017).
53. Yu, A. M. et al. Computationally reconstructing cotranscriptional RNA folding from experimental data reveals rearrangement of non-native folding intermediates. *Mol. Cell* **81**, 870–883.e810 (2021).
54. Cheng, L., White, E. N., Brandt, N. L., Yu, A. M., Chen, A. A. & Lucks, J. B. Cotranscriptional RNA strand exchange underlies the gene regulation mechanism in a purine-sensing transcriptional riboswitch. *Nucleic Acids Res.***50**, 12001–12018 (2022).
55. Uhm, H., Kang, W., Ha, K. S., Kang, C. & Hohng, S. Single-molecule FRET studies on the cotranscriptional folding of a thiamine pyrophosphate riboswitch. *Proc. Natl Acad. Sci. USA* **115**, 331–336 (2018).
56. Rodgers, M. L. & Woodson, S. A. Transcription increases the cooperativity of ribonucleoprotein assembly. *Cell* **179**, 1370–1381.e1312 (2019).
57. Duss, O., Stepanyuk, G. A., Puglisi, J. D. & Williamson, J. R. Transient protein-RNA interactions guide nascent ribosomal RNA folding. *Cell* **179**, 1357–1369.e1316 (2019).
58. Jumper, J. et al. Highly accurate protein structure prediction with AlphaFold. *Nature* **596**, 583–589 (2021).
59. Matsumoto, S. et al. Extraction of protein dynamics information from cryo-EM maps using deep learning. *Nat. Mach. Intell.* **3**, 153–160 (2021).
60. Rames, M., Yu, Y. & Ren, G. Optimized negative staining: a high-throughput protocol for examining small and asymmetric protein structure by electron microscopy. *J. Vis. Exp.***90**, e51087 (2014).
61. Zhang, L. et al. An optimized negative-staining protocol of electron microscopy for apoE4 POPC lipoprotein. *J. Lipid Res.* **51**, 1228–1236 (2010).
62. Sun, M. et al. Practical considerations for using K3 cameras in CDS mode for high-resolution and high-throughput single particle cryo-EM. *J. Struct. Biol.* **213**, 107745 (2021).
63. Mastronarde, D. N. Automated electron microscope tomography using robust prediction of specimen movements. *J. Struct. Biol.* **152**, 36–51 (2005).
64. Zheng, S. Q. et al. MotionCor2: anisotropic correction of beam-induced motion for improved cryo-electron microscopy. *Nat. Methods* **14**, 331–332 (2017).
65. Zhang, K. Gctf: Real-time CTF determination and correction. *J. Struct. Biol.* **193**, 1–12 (2016).
66. Fernandez, J. J., Li, S. & Crowther, R. A. CTF determination and correction in electron cryotomography. *Ultramicroscopy* **106**, 587–596 (2006).
67. Ludtke, S. J., Baldwin, P. R. & Chiu, W. EMAN: semiautomated software for high-resolution single-particle reconstructions. *J. Struct. Biol.* **128**, 82–97 (1999).
68. Pettersen, E. F. et al. UCSF Chimera–a visualization system for exploratory research and analysis. *J. Comput. Chem.* **25**, 1605–1612 (2004).
69. Beckmann, R. et al. Alignment of conduits for the nascent polypeptide chain in the ribosome-Sec61 complex. *Science* **278**, 2123–2126 (1997).
70. Bottcher, B., Wynne, S. A. & Crowther, R. A. Determination of the fold of the core protein of hepatitis B virus by electron cryomicroscopy. *Nature* **386**, 88–91 (1997).
71. Zhang, L. et al. Structural basis of transfer between lipoproteins by cholesteryl ester transfer protein. *Nat. Chem. Biol.* **8**, 342–349 (2012).
72. Wang, S. T. et al. Designed and biologically active protein lattices. *Nat. Commun.* **12**, 3702 (2021).
73. Zhang, X. et al. 3D structural fluctuation of IgG1 antibody revealed by individual particle electron tomography. *Sci. Rep.* **5**, 9803 (2015).
74. Tong, H. et al. Peptide-conjugation induced conformational changes in human IgG1 observed by optimized negative-staining and individual-particle electron tomography. *Sci. Rep.* **3**, 1089 (2013).
75. Zhang, L. et al. Three-dimensional structural dynamics and fluctuations of DNA-nanogold conjugates by individual-particle electron tomography. *Nat. Commun.* **7**, 11083 (2016).
76. Yu, Y. et al. Polyhedral 3D structure of human plasma very low density lipoproteins by individual particle cryo-electron tomography1. *J. Lipid Res.* **57**, 1879–1888 (2016).
77. Reuter, J. S. & Mathews, D. H. RNAstructure: software for RNA secondary structure prediction and analysis. *BMC Bioinformatics* **11**, 129 (2010).
78. Trabuco, L. G., Villa, E., Mitra, K., Frank, J. & Schulten, K. Flexible fitting of atomic structures into electron microscopy maps using molecular dynamics. *Structure* **16**, 673–683 (2008).
79. Liu, J., Bartesaghi, A., Borgnia, M. J., Sapiro, G. & Subramaniam, S. Molecular architecture of native HIV-1 gp120 trimers. *Nature* **455**, 109–113 (2008).
80. Orzechowski, M. & Tama, F. Flexible fitting of high-resolution x-ray structures into cryoelectron microscopy maps using biased molecular dynamics simulations. *Biophys. J.* **95**, 5692–5705 (2008).
81. Ward, J. H. Hierarchical grouping to optimize an objective function. *J. Am. Stat. Assoc.* **58**, 236–244 (1963).
82. Lu, X. J., Bussemaker, H. J. & Olson, W. K. DSSR: an integrated software tool for dissecting the spatial structure of RNA. *Nucleic Acids Res.* **43**, e142 (2015).
83. Punjani, A., Rubinstein, J. L., Fleet, D. J. & Brubaker, M. A. cryoSPARC: algorithms for rapid unsupervised cryo-EM structure determination. *Nat. Methods* **14**, 290–296 (2017).
84. Bepler, T. et al. Positive-unlabeled convolutional neural networks for particle picking in cryo-electron micrographs. *Nat. Methods* **16**, 1153–1160 (2019).
85. Bharat, T. A. & Scheres, S. H. Resolving macromolecular structures from electron cryo-tomography data using subtomogram averaging in RELION. *Nat. Protoc.* **11**, 2054–2065 (2016).

Acknowledgements

We would like to express our gratitude to Drs. Richard Henderson, Mingdong Dong, Jinghui Tao, and Ms. Amy Ren for their insightful discussions and comments. We also extend our appreciation to Dr. Dan Toso at Cal-Cryo-EM center of QB3-Berkeley for his support in cryo-ET imaging. The work at the molecular foundry, LBNL, was supported by the Office of Science, Office of Basic Energy Sciences of the United States Department of Energy (contract no. DE-AC02-05CH11231). The single particle

analysis data set was collected at the EMBION Cryo-EM Facility at iNANO, Aarhus University, Denmark. We acknowledge following research grants: the US National Institutes of Health grants of R01HL115153, R01GM104427, R01MH077303, and R01DK042667 (G.R., J.L., and M.Z.); Independent Research Fund Denmark grant 9040-00425B (E.S.A. and E.K.S.M.); Canadian Natural Sciences and Engineering Research Council grant 532417 (EKSM); European Research Council (ERC) Consolidator grant 683305 (E.S.A., C.G., E.K.S.M.), and Novo Nordisk Foundation Ascending Investigator grant 0060694 (E.S.A. and C.G.).

Author contributions

Experiments were designed by J.L., G.R., and E.S.A. Sample preparation was carried out by E.K.S.M. and C.G. IPET cryo-ET experiments, including data acquisition and processing, were performed by J.L. SPA cryo-EM data collection and analysis performed by E.K.S.M. The templates for modeling were provided by E.K.S.M., C.G., and E.S.A. IPET cryo-ET models were built by G.R. and J.L., and the models were refined by M.Z. and J.L. Data were interpreted and analyzed by J.L., E.K.S.M., M.Z., C.G., E.S.A., and G.R., the IPET related figures and video were created by J.L. and G.R., while SPA related figures were created by E.K.S.M., C.G., and E.S.A. The initial draft of the manuscript was written by J.L. and G.R., and revised by E.K.S.M., M.Z., C.G., and E.S.A.

Competing interests

The authors declare no competing interests.

Additional information

Supplementary information The online version contains supplementary material available at https://doi.org/10.1038/s41467-024-52914-1.

Correspondence and requests for materials should be addressed to Ebbe Sloth Andersen or Gang Ren.

Peer review information *Nature Communications* thanks the anonymous reviewers for their contribution to the peer review of this work. A peer review file is available.

Reprints and permissions information is available at http://www.nature.com/reprints

Publisher's note Springer Nature remains neutral with regard to jurisdictional claims in published maps and institutional affiliations.

Open Access This article is licensed under a Creative Commons Attribution-NonCommercial-NoDerivatives 4.0 International License, which permits any non-commercial use, sharing, distribution and reproduction in any medium or format, as long as you give appropriate credit to the original author(s) and the source, provide a link to the Creative Commons licence, and indicate if you modified the licensed material. You do not have permission under this licence to share adapted material derived from this article or parts of it. The images or other third party material in this article are included in the article's Creative Commons licence, unless indicated otherwise in a credit line to the material. If material is not included in the article's Creative Commons licence and your intended use is not permitted by statutory regulation or exceeds the permitted use, you will need to obtain permission directly from the copyright holder. To view a copy of this licence, visit http://creativecommons.org/licenses/by-nc-nd/4.0/.

© The Author(s) 2024